

Magnetic activity in the HARPS M-dwarf sample [★]

The rotation-activity relationship for very low-mass stars through R'_{HK}

N. Astudillo-Defru^{1,2,3}, X. Delfosse^{1,2}, X. Bonfils^{1,2}, T. Forveille^{1,2}, C. Lovis³, J. Rameau^{1,2,4}

¹ Univ. Grenoble Alpes, IPAG, F-38000 Grenoble, France

² CNRS, IPAG, F-38000 Grenoble, France

³ Observatoire de Genève, Université de Genève, 51 ch. des Maillettes, 1290 Sauverny, Switzerland

⁴ Département de Physique, Université de Montréal, C.P. 6128 Succ. Centre-Ville, Montréal, QC H3C 3J7, Canada

ABSTRACT

Context. Atmospheric magnetic fields in stars with convective envelopes heat stellar chromospheres, and thus increase the observed flux in the Ca II H&K doublet. Starting with the historical Mount Wilson monitoring program, these two spectral lines have been widely used to trace stellar magnetic activity, and as a proxy for rotation period (P_{rot}) and consequently for stellar age. Monitoring stellar activity has also become essential in filtering out false-positives due to magnetic activity in extra-solar planet surveys. The Ca II emission is traditionally quantified through the R'_{HK} -index, which compares the chromospheric flux in the doublet to the overall bolometric flux of the star. Much work has been done to characterize this index for FGK-dwarfs, but M-dwarfs –the most numerous stars of the Galaxy– were left out of these analyses and no calibration of their Ca II H&K emission to an R'_{HK} exists to date.

Aims. We set out to characterize the magnetic activity of the low and very low-mass stars by providing a calibration of the R'_{HK} -index that extends to the realm of M-dwarfs, and by evaluating the relation between R'_{HK} and the rotation period.

Methods. We calibrated the bolometric and photospheric factors for M-dwarfs to properly transform the S-index (which compares the flux in the Ca II H&K lines to a close spectral continuum) into the R'_{HK} . We monitored magnetic activity through the Ca II H&K emission lines in the HARPS M-dwarf sample.

Results. The R'_{HK} index, like the fractional X-ray luminosity L_X/L_{bol} , shows a saturated correlation with rotation, with saturation setting in around a ten days rotation period. Above that period, slower rotators show weaker Ca II activity, as expected. Under that period, the R'_{HK} index saturates to $\sim 10^{-4}$. Stellar mass modulates the Ca II activity, with R'_{HK} showing a constant basal activity above $0.6M_{\odot}$ and then decreasing with mass between $0.6M_{\odot}$ and the fully-convective limit of $0.35M_{\odot}$. Short-term variability of the activity correlates with its mean level, stars with higher R'_{HK} index show larger R'_{HK} variability, as previously observed for earlier spectral types.

Key words. Stars: activity – Stars: late-type – Stars: rotation – Stars : planetary systems – Techniques: spectroscopic

1. Introduction

Stellar activity generically describes the various observational consequences of enhanced magnetic fields, whether those appear on the stellar photosphere, in the chromosphere, or in the corona. In low mass stars, magnetic fields are in turn believed to originate from dynamo processes (e.g. Parker 1955). Stellar activity is thus used as a diagnostic of the dynamo over a wide range of stellar ages, masses, and rotational periods.

It is well established that a larger fraction of M-dwarfs exhibit evidence of magnetic activity that their more massive Sun-like siblings. The fraction of stars showing H_{α} chromospheric emission (Delfosse et al. 1998) or frequent flare (Hawley & Pettersen 1991; Schmidt et al. 2014a; Hawley et al. 2014) increase when the mass decrease for two reasons. On the one hand, lower mass stars have much longer rotational braking times (Delfosse et al. 1998; Barnes 2003; Delorme et al. 2011) and, on the other lower mass stars show stronger chromospheric and coronae emission for a given rotational period (e.g. Kiraga & Stepień 2007). Spectropolarimetric observations demonstrate

that the more massive ($M_{\star} > 0.5 M_{\odot}$) M-dwarfs with reconstructed magnetic topologies have magnetic fields with strong toroidal component, reminiscent of those of active K and G dwarfs, whereas the lowest mass M-dwarfs exhibit magnetic fields that are mainly poloidal (Morin et al. 2008; Donati et al. 2008). This transition takes place slightly above the theoretical full-convection threshold ($M \sim 0.35 M_{\odot}$), suggesting that the dynamo mechanism might change when the $\alpha\Omega$ process can no longer play a major role as the radiative core becomes negligibly small (Chabrier & Baraffe 2000).

Large scale radial velocity searches for extra-solar planets have helped rejuvenate studies of stellar activity, both because they provide extensive time series of high resolution spectra for large samples of stars and because characterizing the activity of a star is essential to avoid confusing symptoms of that activity with a planetary signal. Magnetic inhibition of surface convection, spots, plages, and other inhomogeneities of the stellar surface, indeed all affect the shape of spectral lines, shifting their centroids, and consequently biasing the measured radial velocity. This unwanted signal is often handled as random noise, part of the so-called *RV-jitter*, and added in quadrature to the known noise sources such as photon noise and instrumental instabilities. It can, however, be coherent over the \sim months-long time scale of the stellar rotation, or over the \sim years-long of a stellar activi-

[★] Based on observations made with the HARPS instrument on the ESO 3.6 m telescope under program IDs 072.C-0488(E), 183.C-0437(A), 072.C-0488, 183.C-0972 and 083.C-1001 at Cerro La Silla (Chile).

ity cycle, and can thus be mistaken for the signature of a planetary companion (e.g. Queloz et al. 2001; Bonfils et al. 2007; Robertson et al. 2014). This has stimulated extensive work to model the effect, identify proxies for its source, and filter it out of the RV time series (Dumusque et al. 2011b,a; Boisse et al. 2011, 2012; Lagrange et al. 2010; Meunier et al. 2010; Meunier & Lagrange 2013; Tuomi et al. 2014).

Emission in the core of the Ca II H&K resonance lines (396.8 nm and 393.4 nm) reflects non-thermal heating in the chromosphere that produces bright plages, and is perhaps the most widely used of these activity diagnostics. The historical Mount Wilson program (Vaughan et al. 1978) intensively monitored this activity proxy for about sixty solar-type stars and quantified stellar activity through the so-called S-index. That index is the ratio between the flux through two triangular band-passes (with 1.09 Å full width at half maximum) centered on the Ca II H&K lines and the flux through two 20 Å-wide rectangular pseudo-continuum band-passes on the violet (V, centered at 3901 Å) and red (R, centered at 4001 Å) sides of the lines (Fig. 1).

The S-index is akin to an equivalent width, and well matched to its initial purpose of quantifying variations in the activity of a given star. It can also be used to compare activity levels within a narrow spectral type bin, but is poorly suited to comparing stars of different spectral types. To account for the variation of the continuum level with spectral type, Middelkoop (1982) and Rutten (1984) introduced the C_{cf} factor, which is the ratio between the fraction of the stellar luminosity emitted in the Ca II H&K lines and the S-index (alternatively, C_{cf} can be thought of as a bolometric correction for a photometric filter defined by the two pseudo-continuum bands of the Mount Wilson system). C_{cf} can be estimated from a broad-band color index, and then used to convert the S-index into the fractional luminosity on the Ca II filters. Calibrations of the C_{cf} factor against a broad-band color have to date focused on FGK-dwarfs, with poor coverage of the M-dwarfs. Furthermore these calibrations tend to use $B-V$ as their color index, which happens to be a poor choice for M-dwarfs: these stars emit little flux in the B band, and their V-flux additionally is sensitive to metallicity (e.g. Delfosse et al. 2000; Bonfils et al. 2005). As a consequence, C_{cf} plotted against $B-V$ has a large scatter for $B-V > 1.2$ (late-K) (Vaughan & Preston 1980, Fig. 3).

The two triangular band-passes of the Mount Wilson system centered on the Ca II H&K lines measure a combination of chromospheric and photospheric emissions. R_{HK} consequently is a fractional luminosity in the Ca II lines, rather than a fractional chromospheric luminosity in those lines. Corrections for the photospheric contribution were first proposed by Blanco et al. (1974) and Linsky & Ayres (1978), but Hartmann et al. (1984) has become the standard reference. They compute an S-index from the spectrum of the photosphere, S_{phot} , which the Middelkoop (1982) color-dependent calibration transforms into a R_{HK} for the photosphere, R_{phot} . R'_{HK} then results as $R'_{HK} = R_{HK} - R_{phot}$. The activity index R'_{HK} is thus the fraction of the stellar bolometric luminosity which the chromosphere emits in the Ca II H&K lines. Full details on the conversion of the S-index into R'_{HK} are given in the Appendix of Noyes et al. (1984).

The R'_{HK} index is well characterized for the FGK-dwarfs (Henry et al. 1996; Santos et al. 2000; Wright et al. 2004; Hall et al. 2007; Isaacson & Fischer 2010; Lovis et al. 2011), and some authors (Strassmeier et al. 2000; Tinney et al. 2002; Jenkins et al. 2006) extrapolated the corresponding C_{cf} and R_{phot} conversion factors to later dwarfs. The validity of such extrapolations to redder colors is however questionable. Two more re-

cent studies proposed better grounded calibrations of the Ca II H&K emission of M-dwarfs. Browning et al. (2010) determined L_{Ca}/L_{bol} from the Ca II H&K equivalent widths of a sample of M-dwarfs, but they chose not to anchor their index on the Mount Wilson R'_{HK} , complicating comparisons with solar-type stars. Mittag et al. (2013) used synthetic spectra computed to provide conversions from S to R'_{HK} , but their use of $B-V$ as the color index is, as discussed above, less than ideal for M-dwarfs.

In the present work we calibrate the C_{cf} and R_{phot} factors as a function of $B-V$, $V-I$, and $I-K$ for the early to mid-M-dwarfs (Sect. 3, 4 and 5). In section 7, we then use the resulting R'_{HK} for the HARPS M-dwarf sample to examine how magnetic activity depends on stellar rotation, while section 8 analyses how R'_{HK} varies with the overall stellar parameters.

2. Observations and data reduction

2.1. HARPS spectra

We used spectra observed with the High Accuracy Radial velocity Planets Searcher (HARPS) installed on the ESO 3.6m telescope at La Silla observatory in Chile. HARPS is a fiber-fed cross-dispersed echelle spectrograph covering the 380-690 nm spectral range with a resolving power of 115,000. The stellar light is injected into a science fiber and a second fiber can be illuminated either by a ThAr lamp for simultaneous calibration or by the sky for subtraction of its emission (Mayor et al. 2003).

In order to obtain a measurement of the fraction of luminosity that M-dwarfs emit from the Ca II H&K line we make a spectrophotometric analysis in using the HARPS spectra.

Since our spectra of M-dwarfs are not flux-calibrated, we need to reference them to those of better characterized stars to calibrate C_{cf} and R_{phot} , and we use spectra of GK-dwarfs for that role. Both the GK and the M stars were originally observed to search for exoplanets through high-precision RV monitoring (Lovis et al. 2011; Bonfils et al. 2012, 2013), with selection criteria described in detail in the above papers. Briefly, the GK-dwarfs are within 50 pc and have low projected rotational velocity $v \sin i < 3 - 4 \text{ km s}^{-1}$; their spectra usually have a signal-to-noise (S/N) ratio above 100 per pixel at 550 nm. Our M-dwarfs sample includes ~ 300 M-dwarfs closer than 20 pc, brighter than $V = 12$ mag and southward of $\delta = 15^\circ$, as well as ~ 40 fainter stars kept from the initial GTO sample ($V < 14$ mag; $d < 11$ pc; $\delta < 15^\circ$; $v \sin i \leq 6.5 \text{ km s}^{-1}$).

The HARPS pipeline (Lovis & Pepe 2007) automatically reduces the spectroscopic images to spectra, making use of calibrations obtained during day time. It then extracts the radial velocity from the cross-correlation (CCF) of the spectrum and a binary mask, which also provides a full-width at half-maximum, a contrast, and a bisector-span. In this work, we start from order-merged and background-subtracted spectra corrected from the motion of the observatory relative to the barycenter of the solar system. We used the stellar radial velocity provided by the pipeline to recenter those spectra to the stellar rest-frame. Finally, we corrected from the instrumental transmittance (normalized to unity) using the ratio between a BT-settle (Allard 2014) theoretical spectrum for the bright ($V=6.88$) G-dwarf HD 223171 and the average of 20 observed spectra of that star. This correction therefore assumes that the transmittance does not vary and is consequently approximate. This however is of little consequence since, as described below, our C_{cf} and R_{phot} of M-dwarfs are anchored on those of solar-type stars having these two parameters well-calibrated and observed under very similar conditions.

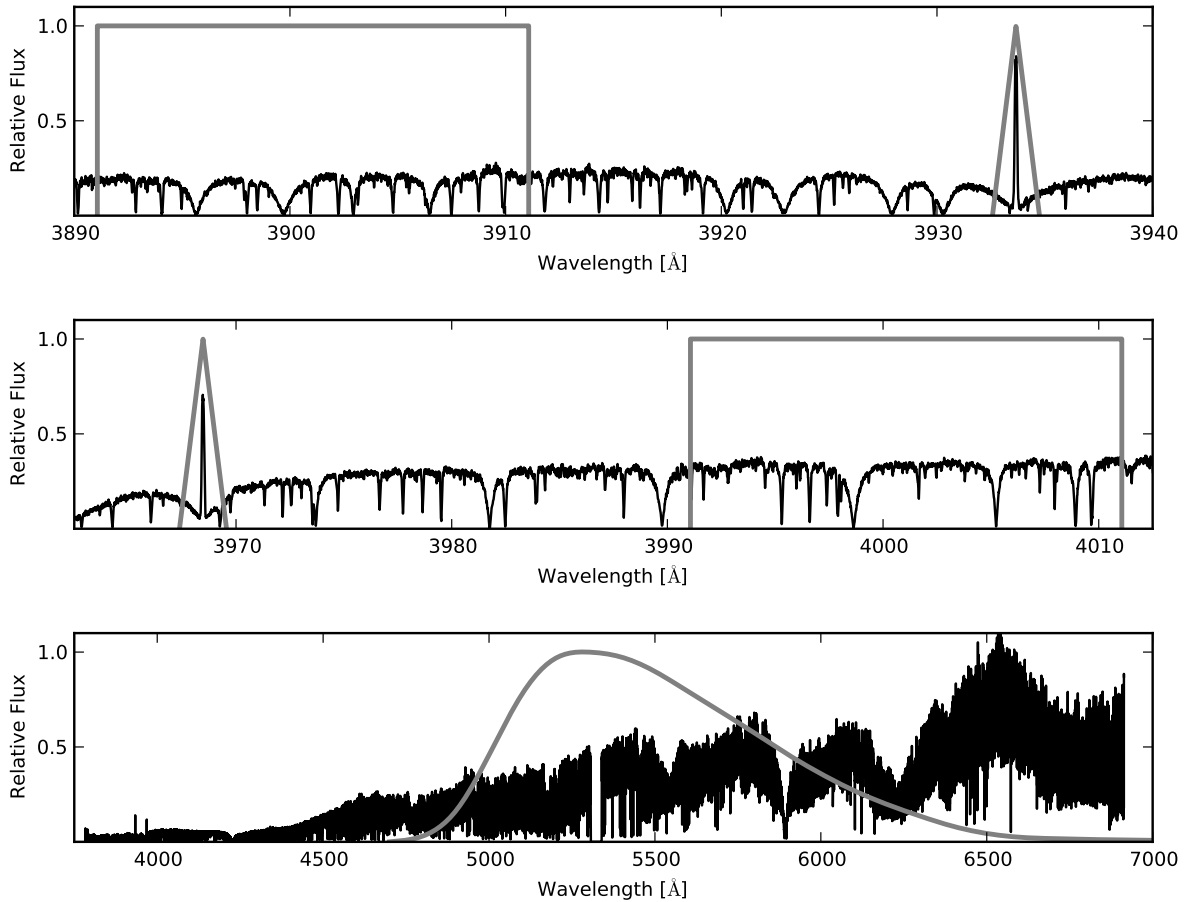


Fig. 1. Median HARPS rest-frame spectrum of a representative mid-M-dwarf (Gl 699) with overlays of the V, K (top panel), and H, R (middle panel) filters of the Mount Wilson system and of the photometric V band (bottom panel)

2.2. Literature photometry, parallaxes, and physical parameters

We obtained BVIK photometry of the M-dwarfs from Leggett (1992), Gaidos et al. (2014) and Cutri et al. (2003); and of the GK-dwarf calibrators from Ducati et al. (2001) and Cutri et al. (2003). When needed, we used the transformations of Carpenter (2001) to homogenize this photometry to the Johnson-Cousins-CIT system. We adopted parallaxes (π) from van Leeuwen (2007), van Altena et al. (1995), Perryman & ESA (1997), Hawley et al. (1997) and the Research Consortium on Nearby Stars (RECONS) parallax program (e.g. Riedel et al. 2010; Jao et al. 2011).

For the GK-dwarfs we adopt the effective temperature, radii, masses, and metallicities listed in Sousa et al. (2008). For the M-dwarfs we obtained the metallicities from Neves et al. (2013), computed effective temperatures and radii using the Boyajian et al. (2012) V-K/metallicity relations, and the stellar masses using the Delfosse et al. (2000) mass vs K-band absolute magnitude relation. The later relation is valid between $0.09M_{\odot}$ and $0.7M_{\odot}$, and the few masses between $0.7M_{\odot}$ and $0.8M_{\odot}$ are therefore based on a slight extrapolation.

3. Scaling the S-index from HARPS observations

The definition of the S-index traces back to the Mount Wilson stellar activity program, and modern measurements are traditionally brought onto the scale defined by that program to ease inter-comparisons. The long-term Mount Wilson program started with a Coudé scanner of the 100-inch telescope (HKP-1) (Wilson 1968, 1978) and later transitioned to a photometer on the 60-inch telescope (HKP-2) (Vaughan et al. 1978).

S is defined as

$$S = \alpha \cdot \frac{f_H + f_K}{f_V + f_R} \quad (1)$$

where f_H , f_K , f_V , and f_R are the total counts in the four passbands described above (Sec. 1 and Fig. 1) and $\alpha=2.4$ is a calibration constant that brings the 100-inch and 60-inch activity indices into approximate agreement.

To compute an S-index with HARPS we choose to follow Lovis et al. (2011) : instead of working with integrated flux in each passband, we use the mean flux per wavelength interval $\tilde{f}_H = f_H/\Delta\lambda_H$, $\tilde{f}_K = f_K/\Delta\lambda_K$, $\tilde{f}_V = f_V/\Delta\lambda_V$ and $\tilde{f}_R = f_R/\Delta\lambda_R$. To be coherent with the Mount Wilson one, our S relationship must be normalized by the ratio of the effective bandpass width $\Delta\lambda_H = \Delta\lambda_K = 1.09 \text{ \AA}$ and $\Delta\lambda_V = \Delta\lambda_R = 20 \text{ \AA}$. In addition, we

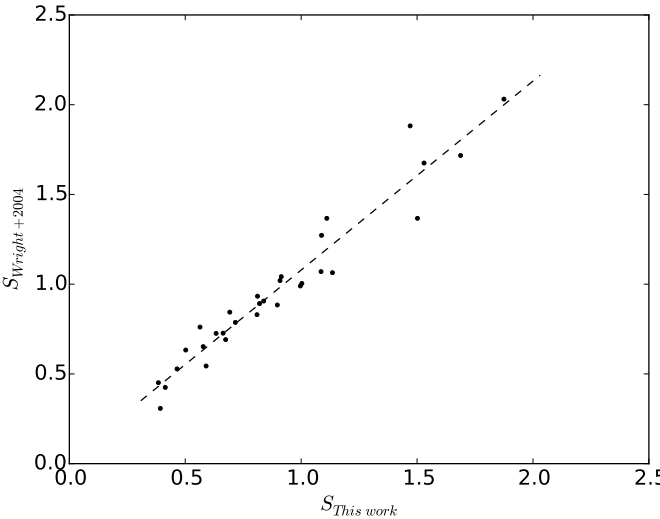


Fig. 2. Median HARPS S-index against the Wright et al. (2004) S-index for the 31 targets in common. The solid line represents the linear least-square fit (Eq. 3) between the two data sets, which we use to bring our S measurements onto the Mount Wilson scale.

must account for the Mount Wilson program's exposing 8 times as long in its narrow H and K bands than in its broader V and R bands, versus our using. The HARPS calibration constant α_H is therefore

$$\alpha_H = \alpha \cdot 8 \cdot \frac{1.09 \text{ \AA}}{20 \text{ \AA}} \sim 1$$

and the S-index can be written as :

$$S \approx \frac{\tilde{f}_H + \tilde{f}_K}{\tilde{f}_V + \tilde{f}_R} \quad (2)$$

We have no target in common with the Mount Wilson program to directly verify the consistency of our S values with its scale, but Wright et al. (2004) scaled their Keck and Lick S-indices to Mount Wilson measurements. We have 31 targets in common with them¹ (Fig. 2), which we use to assess the consistency of the HARPS S-indices with the Mount Wilson scale. The best linear fit between the two datasets is

$$S_{M.W.} = 1.053 \cdot S_{HARPS} + 0.026 \quad (3)$$

The uncertainties in the slope and the intercept from the covariance matrix are 0.0025 and 0.0024, respectively, while the root-mean square deviation of the residuals from that fit, 0.080, is consistent with that expected from variations of the stellar activity between the two non-contemporaneous measurements as illustrated by the dispersion on the S-index obtained by Wright et al. (2004) or those listed in our table A.3. Furthermore the residuals from our fits are higher for large values of the S-index, which is an expected behaviour since more active stars show largest intrinsic variability of the S-index. The small 1.053 factor most likely accounts for minor mismatches between our synthetic filters and the original physical Mount Wilson bandpasses.

¹ The common targets are Gl 465, Gl 357, Gl 1, Gl 581, Gl 87, Gl 667C, Gl 486, Gl 686, Gl 436, Gl 105B, Gl 699, Gl 526, Gl 433, Gl 273, Gl 555, Gl 628, Gl 413.1, GJ 2066, Gl 701, Gl 393, Gl 876, Gl 849, Gl 536, Gl 887, Gl 514, Gl 176, Gl 678.1A, Gl 229, Gl 846, Gl 880, and Gl 382

We use Eq. 3 to bring our S measurements onto the Mount Wilson scale.

R'_{HK} derives from an S-index on the Mount Wilson scale through

$$\begin{aligned} R'_{HK} &= R_{HK} - R_{phot} \\ &= K \cdot \sigma^{-1} \cdot 10^{-14} \cdot C_{cf} \cdot (S - S_{phot}) \end{aligned} \quad (4)$$

where R_{phot} and S_{phot} stand for the photospheric contribution to R and S . C_{cf} is the bolometric factor described in Sec. 1, σ is the Stefan-Boltzmann constant, and 10^{-14} is a scaling factor. K converts the surface fluxes from arbitrary units to physical fluxes on the stellar surface (for a detailed description see, e.g. Rutten 1984, section 2.d). Middelkoop (1982), Rutten (1984), and Hall et al. (2007) respectively find $K = 0.76 \times 10^6$, 1.29×10^6 , 1.07×10^6 [$\text{erg cm}^{-2} \text{ s}^{-1}$]. We use the later value, which is referenced to more recent solar data, hence, $K \cdot \sigma^{-1} \cdot 10^{-14} = 1.887 \times 10^{-4}$.

As discussed in Sec. 1, C_{cf} and R_{phot} were previously poorly constrained in the M-dwarfs domain.

4. The bolometric factor C_{cf}

The bolometric factor is :

$$C_{cf} \equiv \frac{(f_V + f_R)}{f_{bol}} \quad (5)$$

where f_V and f_R are defined in Eq. (1), and f_{bol} is the apparent bolometric flux of the star. Previous works directly applied Equation (5) to FGK-dwarfs to derive a C_{cf} color dependent relation (Middelkoop 1982; Rutten 1984).

Our HARPS M-dwarf spectra are not flux calibrated, and chromatic variations in both seeing (hence fiber injection efficiency) and atmospheric transmission therefore prevent the absolute spectro-photometric computation of f_V , f_R and f_{bol} . However, C_{cf} being a flux ratio, its empirical determination is only concerned by the variation of the transmission (atmospheric and instrumental) in function of the wavelength which can be corrected in using a differential method discussed thereafter.

Since, our spectra were often observed close in time, and in similar condition, to G and K dwarf that can be used to bootstrap the computation through the ratio of the C_{cf} s for the M-dwarf and its G or K standard:

$$\frac{C_{cf,M}}{C_{cf,Std}} = \frac{(f_V + f_R)_M}{(f_V + f_R)_{Std}} \frac{f_{bol,Std}}{f_{bol,M}} \quad (6)$$

where the chromatic components of both atmospheric absorption and injection efficiency cancel out as long as the M-dwarf and its standard star were observed under even moderately similar atmospheric conditions. We stress that the use of \tilde{f}_V , \tilde{f}_R or f_V , f_R (defined above) in Eq. (6) is equivalent.

Since HARPS only observes a small fraction of the spectral energy distribution of our targets, we express f_{bol} as the flux through a standard photometric band covered by the HARPS spectra scaled by a bolometric correction. We choose the standard visual band and write

$$f_{bol} = f_V \times 10^{-0.4BC_V} \quad (7)$$

where BC_V is the bolometric correction for the visual band which is well determined by Flower (1996) for G-K dwarfs and by Leggett et al. (2001) for M-dwarfs, the two relationships adopted in this work.

Combining Eq. 7 and Eq. 6, one obtains:

$$C_{cf,M} = C_{cf,Std} \times \frac{(f_V + f_R)_M}{(f_V + f_R)_{Std}} \frac{f_{V,Std}}{f_{V,M}} \times 10^{-0.4(BC_{V,Std} - BC_{V,M})} \quad (8)$$

To ensure that the G or K spectra are observed under similar atmospheric conditions as the M spectra they are used to pseudo-calibrate, we select pairs of M-dwarf and G or K spectra that were observed

- within 30 min
- at an airmass less than 1.4 for both stars and with an airmass difference less than 0.05
- on a good night, as evaluated by a ratio between the measured and synthetic fluxes in the visual band ($\Sigma = f_V/[t_{exp}10^{-0.4m_V}]$) such that $\Sigma_{Std}/\Sigma_M - 1 \leq 0.2$

The HARPS M-dwarf database contains 14 M-dwarfs that fulfill those criteria. For each target we adopt the median to take an extra precaution allowing to out a eventually imperfectly matched atmospheric conditions despite our selection procedure, and protects against the occasional stellar flare. Table A.1 list the resulting median $\log C_{cf}$, together with the B-V, I-K, and V-K colors.

Figure 3 shows the C_{cf} derived with Eq. (8) against B-V, I-K, and V-K, as well as third order polynomial least-square fits to these data:

$$\log C_{cf} = c_0 X^3 + c_1 X^2 + c_2 X + c_3 \quad (9)$$

where X is one of the color indexes. Table 1 lists the solution for the coefficients of Eq. (9), the number of data points used for the fit, the rms, and the range of validity for each color index. This range of validity corresponds to spectral classes G0 to M6. From the rms values we highlight that the V-K and I-K relations are preferred, but we stress that V-K measurement are generally more available than I-K.

Jenkins et al. (2006) extrapolated the Middelkoop (1982) beyond its B-V<0.9 stated validity range to compute R_{HK} for M-dwarfs. The top panel of Fig. 3 demonstrates that such an extrapolation becomes increasingly invalid for B-V>1.5 and overestimates R_{HK} by up to a factor of three. Our updated C_{cf} -color relation matches the latest main sequence stars in Rutten (1984) quite well and allows to properly compute R_{HK} from S.

5. The photospheric factor R_{phot}

R_{HK} represents the sum of the photospheric and chromospheric fluxes through the two triangular pass-bands (Fig. 1) of the Mount Wilson system. Separating the chromospheric contribution of interest, R'_{HK} , therefore needs a careful estimate of the photospheric flux, R_{phot} . Hartmann et al. (1984) and Noyes et al. (1984) discussed empirical method to determine R_{phot} for the G and K-dwarfs from observed spectra. They use several alternative approaches, all of them consider the photospheric contribution as the flux outside the wavelength domain between the two minimum point in the line profiles of the H and K lines (see Fig. 4 for the K line profile). They conclude that arbitrariness in a number of choices limits the accuracy of the resulting photospheric correction to $\sim 10\%$. More importantly, Noyes et al. (1984) pointed that the photospheric correction becomes unimportant for the coolest stars (B-V $\gtrsim 1.0$) because the reversal emission is very much stronger than the photospheric contribution.

As previous authors (e.g. Walkowicz & Hawley 2009; Mittag et al. 2013) before, we therefore elect to use a theoretical grids

of photospheric model, (here BT-Settl/CIFIST2011bc Allard 2013)² to evaluate the photospheric contribution. Figure 4 illustrates an example of the match between one of these models and the observed spectra of an early-M-dwarf around the Ca II K line.

For each target, we compute $\log g$ from the mass and radius that we respectively obtain from the relations of Delfosse et al. (2000) and Boyajian et al. (2012), we obtain T_{eff} from Boyajian et al. (2012) and [Fe/H] from Neves et al. (2013). We then inspect the model spectra for grid points within $T_{eff} \pm 200$ [K] and $\log(g) \pm 0.5$ [$cm s^{-1}$] and selected that which visually best matches the average observed spectrum of the star between 3880 and 4022 Å. Table 2 lists our computed stellar parameters as well as those of the model that best matches the average spectrum of each star.

We then return to the individual observed spectra and normalize the model spectrum to match them over the wings of (separately) the Ca II H&K lines, which are free of chromospheric emission (Fig. 4). We then replace the central 2 Å region of each Ca II H&K lines by the normalized synthetic spectrum (Fig. 4) to obtain a hybrid spectrum that contains no chromospheric emission, from which we compute S_{phot} using Eq. (2) and (3), and using Eq. (9) for V-K we obtain the photospheric contribution R_{phot} in Eq (4) as:

$$R_{phot} = K \cdot \sigma^{-1} \cdot 10^{-14} \cdot C_{cf} \cdot S_{phot} \quad (10)$$

as explained in Sect. 3: $K \cdot \sigma^{-1} \cdot 10^{-14} = 1.887 \times 10^{-4}$. Table A.1 lists the median of the individual R_{phot} measurements for each M-dwarf and Table A.2 gives this value for our GK-dwarf calibrators.

Figure 5 shows the median R_{phot} obtained against B-V, I-K, and V-K, as well as least-square third order polynomial fits:

$$\log(R_{phot}) = r_0 X^3 + r_1 X^2 + r_2 X + r_3 \quad (11)$$

where X stands for one of the color indexes. The values for the coefficients are tabulated in Table 1, in the same format that described in Sect. 4 for the bolometric factor C_{cf} . The R_{phot} vs V-K relationship show the lowest dispersion.

We note a systematic offset between our measurements and the Hartmann et al. (1984) or Noyes et al. (1984) R_{phot} fits, with their R_{phot} being systematically lower. We suspect that the offset reflects low-level errors in the extrapolation that is intrinsic to a purely empirical estimation of the photospheric flux under a chromospheric line, but it could in principle instead reflect systematics in the theoretical spectra that we use. But we note that our approach is more correct from a physical point of view.

6. Accuracy of the R'_{HK} calibration

The R'_{HK} comes from – as expressed in Eq. (4) – the product of a constant ($K \cdot \sigma^{-1} \cdot 10^{-14}$) and of two factors: C_{cf} and ($S - S_{phot}$). Accuracy and precision of the R'_{HK} calibration is then directly connected to both.

6.1. On the $\log C_{cf}$ accuracy

Our updated $\log C_{cf}$ relationship that include M-dwarfs is purely empirically determined as the product of the C_{cf} of G-K dwarfs calibrators, of the flux ratio between M-dwarfs and G-K dwarfs calibrators in two wavelength domain of our HARPS spectra (V and R calcium pseudo-continuum and standard visual bands),

² <http://phoenix.ens-lyon.fr/Grids/>

Table 1. Solutions for coefficients for the $\log C_{cf}$ -color and R_{phot} -color relationships.

$\log C_{cf}$ Coefficient	$B - V$	$I - K$	$V - K$
c_0	-0.203 ± 0.008	-0.082 ± 0.005	-0.005 ± 0.000
c_1	0.109 ± 0.088	0.416 ± 0.180	0.071 ± 0.000
c_2	-0.972 ± 0.099	-1.544 ± 0.534	-0.713 ± 0.006
c_3	0.669 ± 0.011	0.894 ± 0.120	0.973 ± 0.006
N data points	140	18	81
RMS $\log C_{cf}$	0.102	0.064	0.062
RMS C_{cf}	0.0111	0.0078	0.0088
Valid range	0.54 – 1.9	0.72 – 3.08	1.45 – 6.73
R_{phot} Coefficient	$B - V$	$I - K$	$V - K$
r_0	-0.045 ± 0.033	0.056 ± 0.006	-0.003 ± 0.000
r_1	-0.026 ± 0.392	-0.237 ± 0.188	0.069 ± 0.000
r_2	-1.036 ± 0.470	-0.453 ± 0.547	-0.717 ± 0.003
r_3	-3.749 ± 0.056	-4.099 ± 0.115	-3.498 ± 0.004
R_{phot} data points	78	17	67
$\log(R_{phot})$ RMS	0.104	0.056	0.040
R_{phot} RMS	6.5×10^{-7}	4.4×10^{-7}	3.0×10^{-7}
Valid range	0.54 – 1.9	0.65 – 3.08	1.36 – 6.73

Table 2. Measured stellar parameters, and stellar parameters for the BT-Settl model which best matches the observed spectrum around the Ca II H and K lines.

Name	$\log(g [\text{cm s}^{-1}])$ Det. / Used	$T_{\text{eff}} [\text{K}]$ Det. / Used	Fe/H Det. / Used
Gl 1	5.00 / 5.0	3458 / 3500	-0.45 / -0.5
Gl 191	5.25 / 4.5	3134 / 3300	-0.88 / -1.0
Gl 205	4.70 / 4.5	3780 / 3800	+0.22 / -0.0
Gl 229	4.82 / 5.0	3643 / 3700	-0.10 / -0.0
Gl 393	4.75 / 5.0	3639 / 3600	-0.22 / -0.0
Gl 551	4.94 / 5.0	2659 / 2800	-0.00 / -0.0
Gl 581	4.92 / 5.0	3327 / 3500	-0.21 / -0.0
Gl 588	4.70 / 4.5	3519 / 3500	+0.07 / -0.0
Gl 628	4.80 / 5.0	3364 / 3400	-0.02 / -0.0
Gl 674	4.91 / 5.0	3374 / 3400	-0.25 / -0.5
Gl 699	5.30 / 5.0	3088 / 3300	-0.52 / -0.5
Gl 849	4.59 / 4.5	3519 / 3500	+0.24 / -0.0
Gl 876	4.69 / 4.5	3421 / 3400	+0.15 / -0.0
Gl 887	4.89 / 5.0	3686 / 3700	-0.24 / -0.0

and of a bolometric correction. The internal precision of $\log C_{cf}$ is given in Table 1, with a dispersion of about 0.06 dex. We will discuss here the source of possible systematic errors generating bias.

The $\log C_{cf}$ of G-K dwarfs calibrators is computed with the Middelkoop (1982) relationship whose origins are the Mount Wilson measurements in the 1960ies and 1970ies. It is probable that such factor is too poorly flux calibrated (see the discussion of Mittag et al. 2013) to be considered as an accurate bolometric factor for the V and R calcium pseudo-continuum band. However, that does not impact our study since our goal is to obtain R'_{HK} for M-dwarf that can be compared to the ones of G-K dwarfs. Therefore if we define our C_{cf} relationship as a calibration anchored on its equivalent for G and K-dwarfs, this step does not create a bias.

We compute the ratio of fluxes ³ passing through different bands when deriving the bolometric factor. As described in Sect. 4 we ensure that the G-K standard are observed under similar atmospheric conditions as the M-dwarfs. Thus, if the signal-to-noise of spectra is sufficient this step can only contribute to the dispersion of the C_{cf} . However, under low signal-to-noise conditions an imperfect background subtraction can occur for HARPS reduced spectra and may generate an instrumental systematic. This effect may impact the flux measurements in the V and R calcium pseudo-continuum band and then our C_{cf} calibration. This can be particularly significant for M-dwarfs, due to their low flux at the blue wavelengths of the Ca II H&K lines. Lovis et al. (2011) examine systematics in the HARPS spectrum in this wavelength domain and found that R'_{HK} measurements from HARPS spectra hit an instrumental noise floor only when the S-index photon uncertainty becomes smaller than ~ 0.007 dex. To confirm this behavior we plotted for M-dwarfs of our sample the R'_{HK} standard deviation normalized by R'_{HK} mean value against the average of the S/N ratio (per pixel) in the V and R calcium pseudo-continuum bands ($S/N_{VR,pix}$), and observe that its lower envelope rises systematically for $S/N_{VR,pix} \lesssim 5$. We attribute this rise to systematic, including imperfect background subtraction. To ensure that our C_{cf} calibration is not affected by this effect, we retain only spectra with $S/N_{VR,pix} \geq 5$. It result that the average signal-to-noise of the 14 M-dwarfs and of their comparison G-K-dwarfs we use is ~ 30 (ranging from 7.5 to 57.6). At such level of flux, the effect of the background subtraction is negligible.

R'_{HK} being – in theory – the ratio between the chromospheric emission in the Ca H&K lines and the bolometric flux, we have to use a bolometric correction. For that we use two different bolometric correction relationship: Flower (1996) for G-K dwarfs calibrators and Leggett et al. (2001) for M-dwarfs. Both relation are obtained from flux distribution measurement that is completed by synthetic spectra when certain wavelength domains are uncovered. They use similar zero point (respectively $M_{bol,\odot} = 4.73$ and 4.75). As demonstrated, for example by Flower (1996); Torres (2010) for G-K dwarfs of by Schmidt et al. (2014b); Mann et al. (2015) for M-dwarfs, the agreement among different bolometric corrections is usually better than 0.1 mag. We therefore do not expect that this step might introduce systematic higher than 0.1 mag on $\log C_{cf}$.

To conclude, we are confident that systematic error in our $\log C_{cf}$ for M-dwarfs is negligible.

6.2. Accuracy on $(S - S_{phot})$

It is more difficult to estimate the systematic on S_{phot} , since we use synthetic spectra to reproduce the core of the photospheric Ca II H&K absorption lines. Such line cores can not be measured directly, being always hidden by the chromospheric emission. If the synthetic model does not reproduce them correctly, it will introduce a bias in our R_{phot} relationship. The $\log R_{phot}$ has a dispersion of about 0.05 dex (Table 1).

We make sure that the wings of photospheric Ca II H&K lines is well reproduced by used theoretical spectra (see Fig 4). If, however, the core of the photospheric line is not as well reproduced that the wings, we point that this part of this photospheric contribution cover around 25% of the wavelength domain of the triangular spectrum used to measure S . The used model of the photospheric flux is intermediate between two extreme solution: assume that photospheric flux is 0 under the chromospheric line

³ $C_{cf} \propto [(f_V + f_R)_M / (f_V + f_R)_{std}] / [f_{0,Std} / f_{0,M}]$; from Eq. (8).

or that it is constant and at the level of the reversal points at the basis of the emission line. Therefore our estimation will not be different by more than $\sim 15\%$ that this two extreme solution, Hartmann et al. (1984) have the same conclusion on the effect of different option to estimate S_{phot} . We stress that the use of a synthetic model is today the most physical approach to address this issue.

Furthermore the factor involved in the error budget is ($S - S_{phot}$). In our study the quietest (with lowest Ca II H&K emission) M-dwarf used in the calibration has a S 42% higher than S_{phot} , minimizing the impact of the systematic on S_{phot} to less than 10%. Taking everything into account we estimate that the effect of such systematic is below 0.1 mag on $\log R'_{HK}$.

7. R'_{HK} versus rotation

For low mass star the magnetic field is generated by a combination of (i) $\alpha\Omega$ dynamo (e.g. Parker 1955) taking place under the presence of a radiative core separated from a convective envelope by a strongly sheared thin layer (the tachocline), and (ii) fully convective dynamo (later than M4V; e.g. Bercik et al. 2005) showing similarities with planetary one (Gastine et al. 2013; Schrinner et al. 2014). Stars later than M4V become fully convective (Bercik et al. 2005) and only the second type of dynamo is at work.

On the one hand Zeeman Doppler Imaging of active M-dwarfs indicates that the topology of the large-scale component of their magnetic field changes when they approach the full-convection limit (Donati et al. 2008; Morin et al. 2008), on the other no obvious change at the fully-convective transition is noticeable in the relation between the rotational period and the average field strength (Reiners & Basri 2007; Reiners et al. 2009), or its proxies such as magnetic activity (e.g. L_X Kiraga & Stepień 2007).

Here we analyze how R'_{HK} varies with stellar rotation around the fully convective limit. We use 38 M1 to M6 dwarfs with known stellar rotation periods, inferred from either photometric periodicities or periodic modulation of the S-index. The majority of periods are obtained from the literature (Table 3), but that for 7 M dwarfs are inferred from strong peaks (above 0.3%FAP) in their respective periodogram (e.g. Zechmeister & Kürster 2009) of our measurements of its Ca II H&K emission (GJ 3138, Gl 654, Gl 752A, Gl 876, Gl 880, Gl 382, Gl 514). Both C_{cf} and R_{phot} correlate with similar level of dispersion with either $V - K$ or $I - K$ (Table 1). The dispersion is superior in the correlation with $B - V$. To compute R'_{HK} we use hereafter $\log C_{cf}(V - K)$ and $\log R_{phot}(V - K)$ relationships because in general $V - K$ photometry is more available than $I - K$.

For solar type stars, $\log(R'_{HK})$ correlates with the Rossby number ($Ro = P_{obs}/\tau_c$, where τ_c is the convective overturn time) than with P_{rot} alone (Noyes et al. 1984). This matches the theoretical expectation that the strength of an $\alpha\Omega$ dynamo-process is proportional to Ro^{-2} . Ro is therefore widely used when relating magnetic activity with rotation, though some authors argue that P_{rot} should be preferred (Stepień 1993; Reiners et al. 2014). τ_c can be determined either empirically (e.g. Noyes et al. 1984) or theoretically (e.g Ventura et al. 1998), with both approaches giving uncertain results for M-dwarfs.

Fig. 6 demonstrates that $\log(P_{rot})$ correlates tightly with $\log(R'_{HK})$ for stellar masses between $0.1M_\odot$ and $0.8M_\odot$. Above a ~ 10 days rotation period, activity decreases with slower rota-

tion, while below that period it no longer depends on rotation. The $\log(R'_{HK})$ - $\log(P_{rot})$ relation is well described by:

$$\log(R'_{HK}) = \begin{cases} -1.509 \cdot \log(P_{rot}) - 2.550 & \text{if } P_{rot}[d] > 10 \\ -4.045 & \text{if } P_{rot}[d] < 10 \end{cases} \quad (12)$$

where the $\log(R'_{HK})$ average for the saturated regime does not account for the three stars with masses below $0.2M_\odot$ (GJ 3379, Gl 729, G141-29; see justification below), and Gl 551 is not considered for the non-saturated fit as it shows flares with a significant higher cadence than their siblings with about the same age – rotational period (e.g. Davenport et al. 2016). The $\log(R'_{HK})$ uncertainty is ± 0.093 if $P_{rot}[d] < 10$. For $P_{rot}[d] > 10$, the slope and the y-intercept uncertainties from the fit are respectively ± 0.007 and ± 0.020 . The rms of the non-saturated regime in Eq. (12) is 7.68 days.

Activity saturation in fast M-dwarf rotators is a well known behavior observed in many proxies $L_{H\alpha}/L_{bol}$, L_X/L_{bol} or B_f (e.g. Delfosse et al. 1998; Kiraga & Stepień 2007; Reiners et al. 2009, 2012), and is interpreted either as a physical saturation of the dynamo process or as active regions completely covering the stellar surface while the magnetic field still grows. For M-dwarfs, R'_{HK} saturates at $Ro \approx 0.1$ (adopting here $\tau_c = 70$ d, following Reiners et al. 2009). L_X/L_{bol} and B_f similarly saturate for $Ro \approx 0.1$ (Kiraga & Stepień 2007; Reiners et al. 2009). Above 10 days and out to ~ 100 days, $\log(R'_{HK})$ varies linearly with $\log(P_{rot})$, as also observed for FGK-dwarfs (Noyes et al. 1984; Mamajek & Hillenbrand 2008).

11 of our 38 M-dwarfs have masses under the $0.35M_\odot$ full convection limit. They therefore have no tachocline and consequently cannot operate an $\alpha\Omega$ dynamo. Fig. 6 demonstrates that the $\log(R'_{HK})$ vs. $\log(P_{rot})$ relation does not markedly change at this transition, and that stellar rotation continue to drives activity in fully convective stars. We note that the three lowest mass stars in the saturated half of Fig. 6 have lower $\log(R'_{HK})$ than their more massive counterparts. These three M-dwarfs were not considered for the saturated fit as we suspect that they may follow a different regime. However a larger sample will be needed to confirm if the $\log(R'_{HK})$ level in the saturated regime is correlated with stellar mass for mid to late-M dwarfs.

8. R'_{HK} for the HARPS M-dwarf sample

We computed R'_{HK} for 403 M-dwarfs observed by HARPS for planet searches (Bonfils et al. 2012, 2013). To estimate C_{cf} and R_{phot} we used the V–K relation for Eqs. 9 and 11 when a measurement of that color index is available in the literature, and we backed up to using the B–V relation for Eqs. 9 and 11 when is the only color available.

Table A.3 lists the median of the individual R'_{HK} measurements for each star, which was used for the following analysis. The most active M-dwarfs are fast rotators and, as such were rejected from the planet search programs by the projected rotational velocity cut mentioned in Sect. 2. Our sample is thus biased against the most active M-dwarfs (but it nevertheless includes some of them) and representative of quiet and moderately active M-dwarfs. Accordingly our sample can not be used to estimate the fraction of active stars among the M-dwarfs, however, this is not a limitation to study the correlation between stellar parameters and stellar activity.

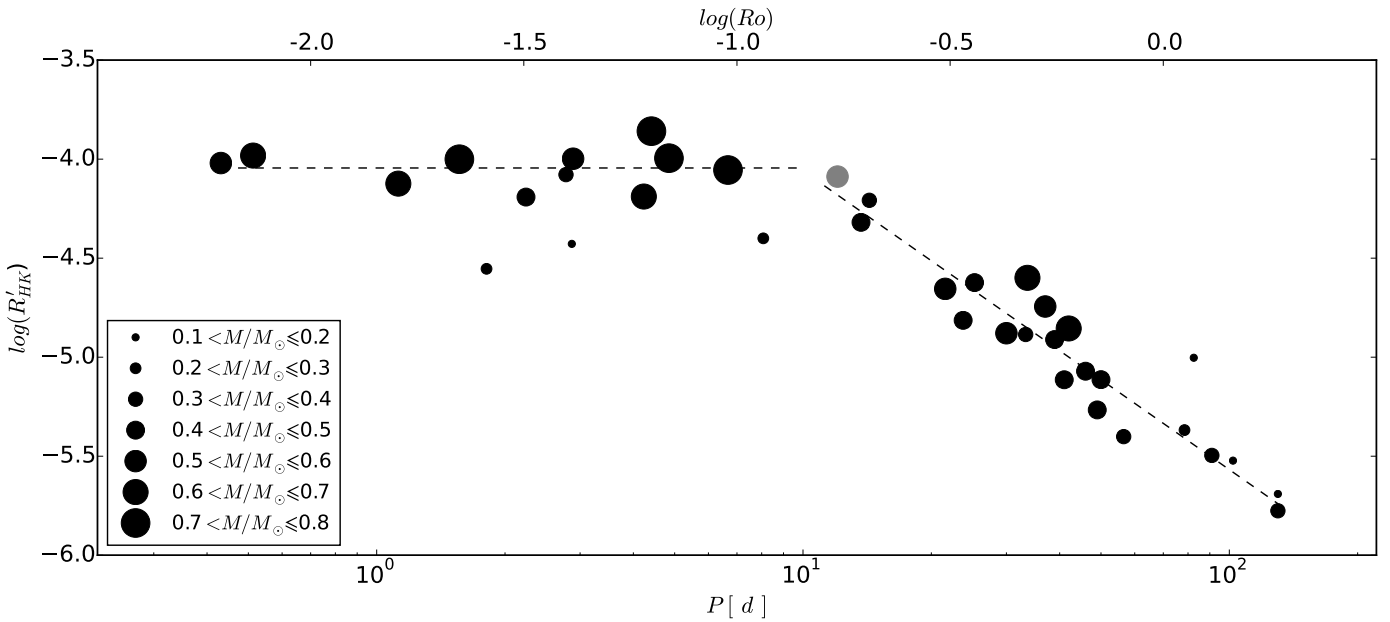


Fig. 6. $\log(R'_HK)$ against rotation period. The area of the filled circles is proportional to the stellar mass, with the grey circle representing one star that only has a photometric parallax (Lépine & Gaidos 2011) and consequently a poorly determined mass. $\log(R'_HK)$ saturates for $P_{\text{rot}} < 10$ days, and then decreases as an approximately linear function of $\log(P_{\text{rot}})$. For illustration, the upper x-axis displays the Rossby number ($Ro = P_{\text{rot}}/\tau_c$) for an assumed $\tau_c = 70$ d.

8.1. R'_HK and metallicity

We first examined R'_HK against metallicity (Fig. 7). Metallicity affects R'_HK measurements of the warmer solar type stars, because, at a given T_{eff} , metal-poor stars have weaker fluxes in the V and R pseudo-continuum pass-bands, and therefore higher S values for the same Ca II H&K flux; metallicity also affects the C_{cf} factor, which is derived from the flux in the visual band, which in turn is sensitive to metallicity. Lovis et al. (2011) noticed from a linear trend in the lower envelope of a R'_HK versus Fe/H diagram that R'_HK systematically decreases as Fe/H increases, and find that taking into account the variation of the bolometric flux as a function of Fe/H eliminates that trend (their Fig. 3). Fig. 7 demonstrates that the lower envelope of the M-dwarf diagram shows no such trend, and we therefore include no metallicity term in our R'_HK calibration. One can also note that the active M-dwarfs cluster in the metal-rich side of the diagram, as qualitatively expected from combination of the age-metallicity correlation and the decreasing chromospheric activity of older stars. Solar-metallicity M-dwarfs of our sample nonetheless show $\log R'_HK$ ranging from -6.0 to -4.25 while their FGK counterparts are less dispersed with $\log R'_HK$ ranging from -5.1 to -4.65. Knowing that the most active stars have been rejected in our M-dwarfs sample, the $\log R'_HK$ dispersion for these stars might even be stronger. This could be originate from the longer spin-down timescales of M-dwarfs and, therefore it takes a longer time before all the stars converge to the sequence of the lower rotators.

8.2. Dispersion of the R'_HK epoch measurements

The dispersion of the individual R'_HK measurements of a star contains contributions from true stellar variability, instrumental systematic, and noise. As discussed in Sec. 6 the later can often be dominant for M-dwarfs, due to their low flux at the blue wavelengths of the Ca II H&K. To minimize this effect we re-

strict discussion on variability to stars for which at least six R'_HK measurement have $S/N_{VR, \text{pix}} \geq 5$ (see Sec. 6 for more details).

Figure 8 displays the median R'_HK against its dispersion and shows that the more active stars are more variable, as is also true for GK-dwarfs (e.g. Lovis et al. 2011). Many of the most active stars in Figure 8 are known flare-stars, including Gl 551 (Proxima Centauri), Gl 54.1, Gl 729, GJ 3379, GJ 234AB, and GJ 3148A. The most likely R'_HK dispersion for an M-dwarf is 1.2×10^{-6} , while the peak of the distribution is located at 0.6×10^{-6} , 3 times higher than the 0.2×10^{-6} for GK-dwarfs, and the M-dwarf histogram is also broader. This may stem from the slower spin-down of the M-dwarfs, although residual instrumental effects could perhaps contribute.

Such strongest intrinsic variability of the M-dwarfs activity has often been pointed, but few quantified until now. Such variability also concerns quiet M-dwarfs.

8.3. Activity as a function of stellar mass

We now turn our attention to the relation between magnetic activity and stellar mass, restricting the discussion to stars with a well measured parallax ($\delta\pi/\pi < 0.1$) and for which a mass can therefore be inferred from the Delfosse et al. (2000) mass vs M_K relation. We first consider three mass bins, $M/M_{\odot} \leq 0.4$, $0.4 < M/M_{\odot} \leq 0.6$, and $0.6 < M/M_{\odot} < 0.8$. Fig. 9 presents histograms of the median $\log(R'_HK)$ for each bin, and shows that most likely activity level decreases with stellar mass. The histogram for the highest mass bin peaks at $\log(R'_HK) = -4.84$ – slightly higher than the -4.95 observed for GK-dwarfs Lovis et al. (2011) –, that for the intermediate mass bin peaks around -5.19, while that for the lowest mass bin peaks at -5.47 but displays a strong tail of more active stars retained from our sample selection.

For an unbinned view, Fig. 10 displays R'_HK as a function of stellar mass. Both the lower envelope and the mode of the R'_HK distribution are approximately flat above $\sim 0.6M_{\odot}$, decrease with mass between $\sim 0.6M_{\odot}$ and $\sim 0.35M_{\odot}$, and flatten again below

Table 3. The $\log R'_{HK}$ – fourth column – and rotation periods – fifth column – of the 38 M-dwarfs for which both are known. Their reference are given in sixth column: (1) Kiraga & Stepień (2007), (2) Bonfils et al. (2013), (3) Morin et al. (2008), (4) Irwin et al. (2011), (5) Robertson et al. (2014), (6) Astudillo-Defru et al. (2015), and (7) this work. Seventh column gives the rotation periods derived from Eq. (12), where objects flagged with (*) are the three very low mass stars showing the lowest $\log(R'_{HK})$ in the saturated regime (Fig. 6). The rms of $P_{Rot.}$ and $P_{Rot. Fit}$ is 12 days. V-K color and stellar mass are tabulated respectively in second and third columns.

Name	V-K [mag]	M [M_\odot]	$\log(R'_{HK})$	$P_{Rot.}$ [d]	$P_{Ref.}$	$P_{Rot. Fit}$ [d]
GJ 1264	4.288	0.74	-4.055	6.67	(1)	≤ 10
Gl 699	5.040	0.16	-5.691	130	(1)	121
Gl 569A	4.416	0.48	-4.319	13.68	(1)	15
GJ 182	3.680	0.79	-3.859	4.41	(1)	≤ 10
GJ 890	3.852	0.57	-4.020	0.43	(1)	≤ 10
GJ 867A	4.716	0.63	-4.189	4.23	(1)	12
GJ 841A	4.769	0.68	-4.124	1.12	(1)	≤ 10
Gl 803	4.230	0.74	-3.995	4.85	(1)	≤ 10
Gl 729	5.080	0.17	-4.428	2.87	(1)	18 (*)
Gl 618A	4.686	0.38	-5.401	56.52	(1)	78
Gl 551	6.730	0.12	-5.003	82.53	(1)	42
GJ 494	4.150	0.60	-3.998	2.89	(1)	≤ 10
GJ 431	4.980	0.37	-4.208	14.31	(1)	13
GJ 3367	3.817	0.54	-4.088	12.05	(1)	≤ 10
GJ 1054A	3.949	0.66	-3.982	0.51	(1)	≤ 10
GJ 103	3.941	0.75	-4.000	1.56	(1)	≤ 10
Gl 205	4.080	0.63	-4.599	33.61	(1)	23
Gl 358	4.660	0.42	-4.623	25.26	(1)	24
Gl 176	4.509	0.49	-4.911	38.92	(1)	37
Gl 674	4.480	0.34	-4.885	33.29	(1)	35
Gl 479	4.640	0.43	-4.814	23.75	(2)	32
Gl 526	4.010	0.49	-5.113	50.00	(2)	50
Gl 388	4.710	0.42	-4.191	2.24	(3)	≤ 10
Gl 12	4.809	0.22	-5.368	78.50	(4)	74
G 141-29	5.235	0.24	-4.400	8.07	(4)	17 (*)
GJ 3379	5.334	0.23	-4.554	1.81	(4)	21 (*)
GJ 1057	5.950	0.18	-5.522	102.00	(4)	93
LHS 1610	5.783	0.17	-5.375	78.80	(4)	75
Gl 285	5.420	0.31	-4.078	2.78	(4)	≤ 10
Gl 581	4.710	0.31	-5.776	130	(5)	137
GJ 3293	4.520	0.52	-5.114	41	(6)	50
GJ 3138	3.710	0.68	-4.855	42	(7)	34
Gl 654	4.120	0.48	-5.266	49	(7)	63
Gl 752A	4.460	0.49	-5.071	46	(7)	47
Gl 876	5.120	0.33	-5.496	91	(7)	90
Gl 880	4.130	0.58	-4.744	37	(7)	28
Gl 382	4.170	0.53	-4.655	22	(7)	25
Gl 514	3.990	0.52	-4.879	30	(7)	35

$\sim 0.35M_\odot$. The later break approximately coincides with the transition from partially to fully convective stars (Chabrier & Baraffe 2000), and could potentially reflect a change at this transition where the $\alpha\Omega$ dynamo vanishes and that a change is observed in the topology of the large-scale component of their magnetic field (Donati et al. 2008; Morin et al. 2008).

For the earlier spectral types, our findings are consistent with those of Mittag et al. (2013). They found that Ca II activity rises over $1.1 \leq B-V \leq 1.3$ (K5 to K7-dwarfs) and decreases over $1.3 \leq B-V \leq 1.5$ (M0 to M3-dwarfs), but could not establish whether that decrease continues to later spectral types since their sample does not extend beyond M3. Fig. 5 in Browning et al.

(2010) shows a similar behavior of L_{Ca}/L_{Bol} against spectral type for M-dwarfs, albeit less clearly.

$H\alpha$ shows a similar behavior although the decline starts at mid-M-dwarfs. $L_{H\alpha}/L_{bol}$ remains approximately constant for spectral types M0 to M5 and only starts declining at M5-M6 (West et al. 2004). This is not inconsistent, since Ca II H&K and $H\alpha$ trace different chromospheric heights. Their emissions do positively correlate for very active stars, but not for intermediate or weak activity stars (Rauscher & Marcy 2006; Walkowicz & Hawley 2009).

9. Conclusions and summary

We use high-resolution spectra of M-dwarf observed in HARPS planet-search programs to analyse their Ca II H&K magnetic activity and examine how it varies with stellar rotation period, stellar mass, and color. For this purpose, we extend the B-V photometric calibrations of the bolometric C_{cf} and photospheric R_{phot} factors used in the computation of the R'_{HK} -index to $B-V=1.90$ (spectral type M6). We also derive alternative, and preferred, I-K and V-K calibrations of these two factors.

We calibrated the C_{cf} relationship from a purely empirical way, without the use of synthetic spectra, through the integrated flux in the V and R control bands, and the bolometric flux determined by the integrated flux in the visual band and the bolometric correction (Flower 1996; Leggett et al. 2001). On the contrary the R_{phot} relationship is calibrated in using a synthetic spectrum that replace a narrow window (2 Å) around Ca II H&K lines of observed spectra (chromosphere+photosphere). While an extrapolation of the Rutten (1984) C_{cf} vs B-V relation agrees reasonably well with our new relation for $B-V < 1.6$, we find that extrapolating the Middelkoop (1982) or Noyes et al. (1984), as done by Tinney et al. (e.g. 2002); Jenkins et al. (e.g. 2006) overestimates R'_{HK} values by factors of 2 to 3 for mid to late-M-dwarfs.

The $\log(R'_{HK})$ vs. $\log(P_{rot})$ diagram of M0-M6 dwarfs displays two distinct regimes, with $\log(R'_{HK})$ saturated for $P < 10$ d (or a Rossby number of ≈ 0.1 for an assumed $\tau_c = 70$ d convective turnover timescale) and then decreasing as a linear function of $\log(P_{rot})$ for longer rotational periods. These two regimes similarly appear in other tracers of magnetic activity (like L_X/L_{bol} or B_f , Kiraga & Stepień 2007; Reiners et al. 2009). R'_{HK} , L_X/L_{bol} , and B_f all depend similarly on stellar rotation in the unsaturated regime, as expected if rotation drives all magnetic activity. The stellar rotation can be estimated from L_X/L_{bol} (e.g. Kiraga & Stepień 2007), although R'_{HK} has the potential to derive P_{rot} for quieter stars, where X emission is eventually not detected.

The lower envelope of the Ca II H&K activity varies with mass over the M-dwarf range. The basal level of the R'_{HK} distribution decrease with the lower envelope and mode of the R'_{HK} distribution decreasing with stellar mass down to $M \sim 0.35M_\odot$ and flattening below that mass, which coincides with the transition from partially to fully convective stars. It will be difficult to confirm if another basal corona and chromosphere emission decrease with mass for M-dwarfs, $L_{H\alpha}/L_{BOL}$ or L_X/L_{BOL} being not determined for the quietest stars.

Besides insight on surface magnetic fields, Eq. (12) provides information on P_{rot} (with a typical accuracy of 8 days) from a measurement of R'_{HK} that can be obtained from a single high resolution spectrum. This has significant practical importance in the context of extra-solar planet searches, where stellar activity modulated by rotational visibility is an important source of false-positives (e.g. Bonfils et al. 2007; Robertson et al. 2014). A good

estimate of P_{rot} from Eq.(12) can thus retire false positive worries when the potential signal is sufficiently removed from the estimated stellar rotation period and its harmonics (Boisse et al. 2011), and will intensify such worries when it is not.

Acknowledgements. The authors acknowledge Nadège Meunier and Eduardo Martín for theirs precious comments. N. A.-D. acknowledges support from CONICYT Becas-Chile 72120460. X. B., X. D., and T. F. acknowledge the support of the French Agence Nationale de la Recherche (ANR), under the program ANR-12-BS05-0012 Exo-atmos and of PNP (Programme national de planétologie). This work has been partially supported by the Labex OSUG@2020. X.B. acknowledges funding from the European Research Council under the ERC Grant Agreement n. 337591-ExTrA.

References

- Allard, F. 2013, in Proceedings of the International Astronomical Union, Vol. 8, Exploring the Formation and Evolution of Planetary Systems, 271–272
- Allard, F. 2014, in IAU Symposium, Vol. 299, IAU Symposium, ed. M. Booth, B. C. Matthews, & J. R. Graham, 271–272
- Astudillo-Defru, N., Bonfils, X., Delfosse, X., et al. 2015, A&A, 575, A119
- Barnes, S. A. 2003, ApJ, 586, 464
- Bercik, D. J., Fisher, G. H., Johns-Krull, C. M., & Abbott, W. P. 2005, ApJ, 631, 529
- Blanco, C., Catalano, S., Marilli, E., & Rodonò, M. 1974, A&A, 33, 257
- Boisse, I., Bonfils, X., & Santos, N. C. 2012, A&A, 545, A109
- Boisse, I., Bouchy, F., Hébrard, G., et al. 2011, A&A, 528, A4
- Bonfils, X., Delfosse, X., Udry, S., et al. 2013, A&A, 549, A109
- Bonfils, X., Delfosse, X., Udry, S., et al. 2005, A&A, 442, 635
- Bonfils, X., Gillon, M., Udry, S., et al. 2012, A&A, 546, A27
- Bonfils, X., Mayor, M., Delfosse, X., et al. 2007, A&A, 474, 293
- Boyajian, T. S., von Braun, K., van Belle, G., et al. 2012, ApJ, 757, 112
- Browning, M. K., Basri, G., Marcy, G. W., West, A. A., & Zhang, J. 2010, AJ, 139, 504
- Carpenter, J. M. 2001, AJ, 121, 2851
- Chabrier, G. & Baraffe, I. 2000, ARA&A, 38, 337
- Cutri, R. M., Skrutskie, M. F., van Dyk, S., et al. 2003, VizieR Online Data Catalog, 2246, 0
- Davenport, J. R. A., Kipping, D. M., Sasselov, D., Matthews, J. M., & Cameron, C. 2016, ApJ, 829, L31
- Delfosse, X., Forveille, T., Perrier, C., & Mayor, M. 1998, A&A, 331, 581
- Delfosse, X., Forveille, T., Ségransan, D., et al. 2000, A&A, 364, 217
- Delorme, P., Collier Cameron, A., Hebb, L., et al. 2011, MNRAS, 413, 2218
- Donati, J.-F., Morin, J., Petit, P., et al. 2008, MNRAS, 390, 545
- Ducati, J. R., Bevilacqua, C. M., Rembold, S. B., & Ribeiro, D. 2001, ApJ, 558, 309
- Dumusque, X., Santos, N. C., Udry, S., Lovis, C., & Bonfils, X. 2011a, A&A, 527, A82
- Dumusque, X., Udry, S., Lovis, C., Santos, N. C., & Monteiro, M. J. P. F. G. 2011b, A&A, 525, A140
- Flower, P. J. 1996, ApJ, 469, 355
- Gaidos, E., Mann, A. W., Lépine, S., et al. 2014, MNRAS, 443, 2561
- Gastine, T., Morin, J., Duarte, L., et al. 2013, A&A, 549, L5
- Hall, J. C., Lockwood, G. W., & Skiff, B. A. 2007, AJ, 133, 862
- Hartmann, L., Soderblom, D. R., Noyes, R. W., Burnham, N., & Vaughan, A. H. 1984, ApJ, 276, 254
- Hawley, S. L., Davenport, J. R. A., Kowalski, A. F., et al. 2014, ApJ, 797, 121
- Hawley, S. L., Gizis, J. E., & Reid, N. I. 1997, AJ, 113, 1458
- Hawley, S. L. & Pettersen, B. R. 1991, ApJ, 378, 725
- Henry, T. J., Soderblom, D. R., Donahue, R. A., & Baliunas, S. L. 1996, AJ, 111, 439
- Irwin, J., Berta, Z. K., Burke, C. J., et al. 2011, ApJ, 727, 56
- Isaacson, H. & Fischer, D. 2010, ApJ, 725, 875
- Jao, W.-C., Henry, T. J., Subasavage, J. P., et al. 2011, AJ, 141, 117
- Jenkins, J. S., Jones, H. R. A., Tinney, C. G., et al. 2006, MNRAS, 372, 163
- Kiraga, M. & Stepien, K. 2007, Acta Astron., 57, 149
- Lagrange, A.-M., Desort, M., & Meunier, N. 2010, A&A, 512, A38
- Leggett, S. K. 1992, ApJS, 82, 351
- Leggett, S. K., Allard, F., Geballe, T. R., Hauschildt, P. H., & Schweitzer, A. 2001, ApJ, 548, 908
- Lépine, S. & Gaidos, E. 2011, AJ, 142, 138
- Linsky, J. L. & Ayres, T. R. 1978, ApJ, 220, 619
- Lovis, C., Dumusque, X., Santos, N. C., et al. 2011, ArXiv e-prints
- Lovis, C. & Pepe, F. 2007, A&A, 468, 1115
- Mamajek, E. E. & Hillenbrand, L. A. 2008, ApJ, 687, 1264
- Mann, A. W., Feiden, G. A., Gaidos, E., Boyajian, T., & von Braun, K. 2015, ApJ, 804, 64
- Mayor, M., Pepe, F., Queloz, D., et al. 2003, The Messenger, 114, 20
- Meunier, N., Desort, M., & Lagrange, A.-M. 2010, A&A, 512, A39
- Meunier, N. & Lagrange, A.-M. 2013, A&A, 551, A101
- Middelkoop, F. 1982, A&A, 107, 31
- Mittag, M., Schmitt, J. H. M. M., & Schröder, K.-P. 2013, A&A, 549, A117
- Morin, J., Donati, J.-F., Petit, P., et al. 2008, MNRAS, 390, 567
- Neves, V., Bonfils, X., Santos, N. C., et al. 2013, A&A, 551, A36
- Noyes, R. W., Hartmann, L. W., Baliunas, S. L., Duncan, D. K., & Vaughan, A. H. 1984, ApJ, 279, 763
- Parker, E. N. 1955, ApJ, 122, 293
- Perryman, M. A. C. & ESA, eds. 1997, ESA Special Publication, Vol. 1200, The HIPPARCOS and TYCHO catalogues. Astrometric and photometric star catalogues derived from the ESA HIPPARCOS Space Astrometry Mission
- Queloz, D., Henry, G. W., Sivan, J. P., et al. 2001, A&A, 379, 279
- Rauscher, E. & Marcy, G. W. 2006, PASP, 118, 617
- Reiners, A. & Basri, G. 2007, ApJ, 656, 1121
- Reiners, A., Basri, G., & Browning, M. 2009, ApJ, 692, 538
- Reiners, A., Joshi, N., & Goldman, B. 2012, AJ, 143, 93
- Reiners, A., Schüssler, M., & Passegger, V. M. 2014, ApJ, 794, 144
- Riedel, A. R., Subasavage, J. P., Finch, C. T., et al. 2010, AJ, 140, 897
- Robertson, P., Mahadevan, S., Endl, M., & Roy, A. 2014, Science, 345, 440
- Rutten, R. G. M. 1984, A&A, 130, 353
- Santos, N. C., Mayor, M., Naef, D., et al. 2000, A&A, 361, 265
- Schmidt, S. J., Prieto, J. L., Stanek, K. Z., et al. 2014a, ApJ, 781, L24
- Schmidt, S. J., West, A. A., Bochanski, J. J., Hawley, S. L., & Kielty, C. 2014b, PASP, 126, 642
- Schrinner, M., Petitdemange, L., Raynaud, R., & Dormy, E. 2014, A&A, 564, A78
- Sousa, S. G., Santos, N. C., Mayor, M., et al. 2008, A&A, 487, 373
- Stepien, K. 1993, in IAU Symposium, Vol. 157, The Cosmic Dynamo, ed. F. Krause, K. H. Radler, & G. Rudiger, 141
- Strassmeier, K., Washuettl, A., Granzer, T., Scheck, M., & Weber, M. 2000, A&AS, 142, 275
- Tinney, C. G., McCarthy, C., Jones, H. R. A., et al. 2002, MNRAS, 332, 759
- Torres, G. 2010, AJ, 140, 1158
- Tuomi, M., Anglada-Escude, G., Jenkins, J. S., & Jones, H. R. A. 2014, ArXiv e-prints
- van Altena, W. F., Lee, J. T., & Hoffleit, E. D. 1995, The general catalogue of trigonometric [stellar] parallaxes
- van Leeuwen, F. 2007, A&A, 474, 653
- Vaughan, A. H. & Preston, G. W. 1980, PASP, 92, 385
- Vaughan, A. H., Preston, G. W., & Wilson, O. C. 1978, PASP, 90, 267
- Ventura, P., Zeppieri, A., Mazzitelli, I., & D'Antona, F. 1998, A&A, 334, 953
- Walkowicz, L. M. & Hawley, S. L. 2009, AJ, 137, 3297
- West, A. A., Hawley, S. L., Walkowicz, L. M., et al. 2004, AJ, 128, 426
- Wilson, O. C. 1968, ApJ, 153, 221
- Wilson, O. C. 1978, ApJ, 226, 379
- Wright, J. T., Marcy, G. W., Butler, R. P., & Vogt, S. S. 2004, ApJS, 152, 261
- Zechmeister, M. & Kürster, M. 2009, A&A, 496, 577

Appendix A: Tables

Table A.1. Median values for C_{cf} and for R_{phot} for M-dwarfs. N is the number of spectra satisfying restrictions described in Sect. 4. C_{cf} values are derived from Eq. (8); R_{phot} is obtained with equations (2), (3), (4), and (9) V–K relation after the reversal Ca II H&K emission was replaced by the corresponding BT-Settl spectrum.

Name	N	B-V	I-K	V-K	BC_v	$\log C_{cf}$	$\log(R_{phot})$
Gl 1	28	1.48	1.900	4.030	-1.278	-1.089	-5.529
Gl 191	3	1.56	1.807	3.767	-1.492	-1.161	-5.436
Gl 205	34	1.47	2.010	4.080	-1.698	-1.145	-5.454
Gl 229	7	1.50	1.960	3.970	-1.487	-1.121	-5.374
Gl 393	3	1.51	2.075	4.315	-1.888	-1.235	-5.497
Gl 551	17	1.90	3.080	6.730	-3.808	-2.338	-6.117
Gl 581	50	1.60	2.200	4.710	-2.283	-1.385	-5.654
Gl 588	4	1.53	2.147	4.527	-1.864	-1.331	-5.654
Gl 628	10	1.58	2.301	4.981	-2.064	-1.431	-5.691
Gl 674	38	1.53	2.101	4.480	-2.049	-1.326	-5.628
Gl 699	3	1.73	2.260	5.040	-2.392	-1.558	-5.750
Gl 849	17	1.50	2.262	4.762	-2.357	-1.329	-5.687
Gl 876	17	1.58	2.416	5.146	-3.808	-1.447	-5.803
Gl 887	31	1.50	1.940	3.960	-1.402	-1.131	-5.410

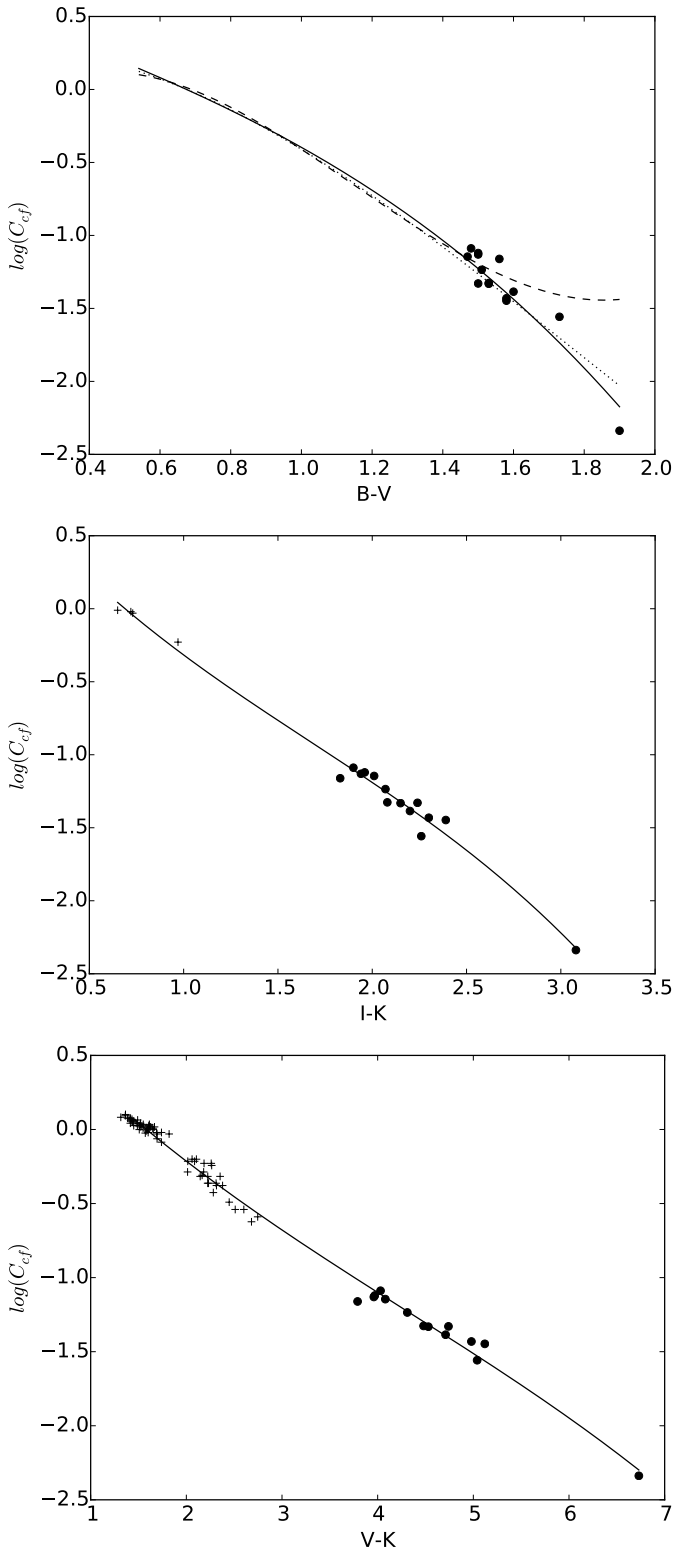


Fig. 3. The C_{cf} bolometric factor against $B-V$ (top panel), $I-K$ (middle panel), and $V-K$ (bottom panel). Black dots represent the $C_{cf,M}$ median, while crosses represent $C_{cf,Std}$. Solid lines represent the least-square fits of Eq. (9) for each color index. The top panel omits the 125 $C_{cf,Std}(B-V)$ data points to more clearly display the Middelkoop (1982) and Rutten (1984) fits, represented by dashed and dotted lines. The validity range of these previous relationships are $0.45 < B-V < 1.50$ and $0.3 < B-V < 1.6$ respectively and, for comparison, are extrapolated in this figure up to the colour index of M-dwarfs.

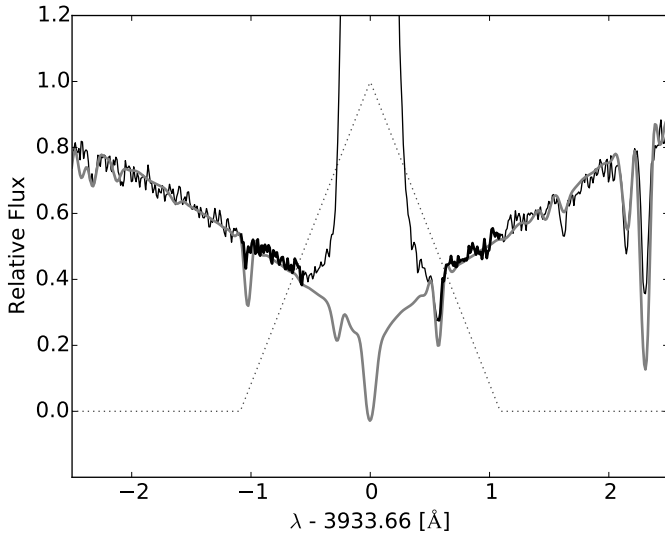


Fig. 4. Spectrum of Gl 205 around the Ca II K line. The thin black and bold grey lines respectively represent the observed spectrum and a BT-Settl theoretical spectrum with $T_{\text{eff}} = 3800$ [K], $\log(g)$ [cm/s] = 4.5, and Fe/H = 0.0. The dotted curve depicts the K filter. The bold black line represents part of the spectral contribution through the triangular K filter used to estimate the photospheric contribution in previous study (Hartmann et al. 1984)

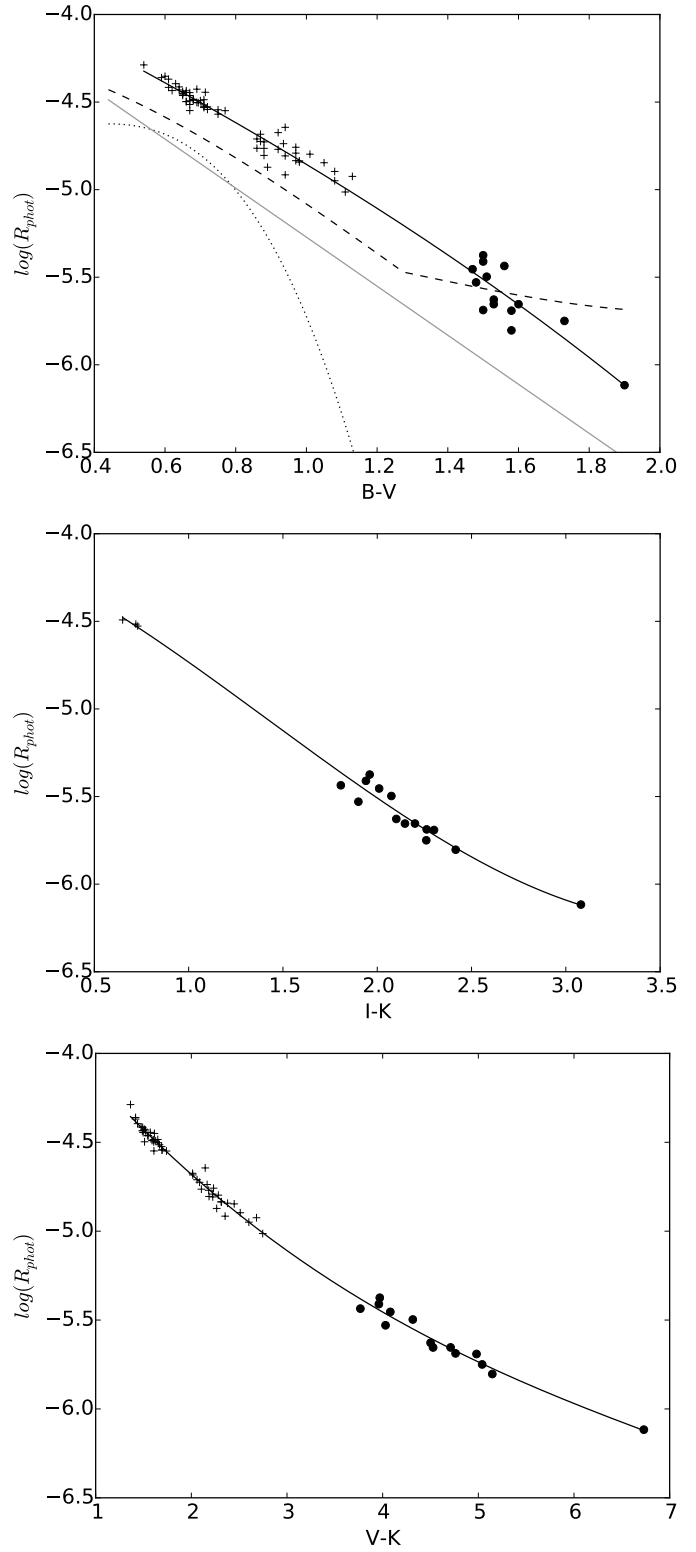


Fig. 5. The photospheric factor as a function of, from top to bottom, B–V, I–K, and V–K. Dots and crosses respectively represent R_{phot} for M and GK-dwarfs. The solid lines are from Eq. (11) for each one of the color indexes. On the top panel we compare our relationship for the B–V colors to the ones of Hartmann et al. (1984), Noyes et al. (1984), and Mittag et al. (2013, only from synthetic spectra) in dotted, dashed, and dash-dotted lines respectively. Their range of validity is $0.44 < B - V < 0.82$ for Hartmann et al. (1984) and Noyes et al. (1984), and $0.44 < B - V < 1.6$ for Mittag et al. (2013).

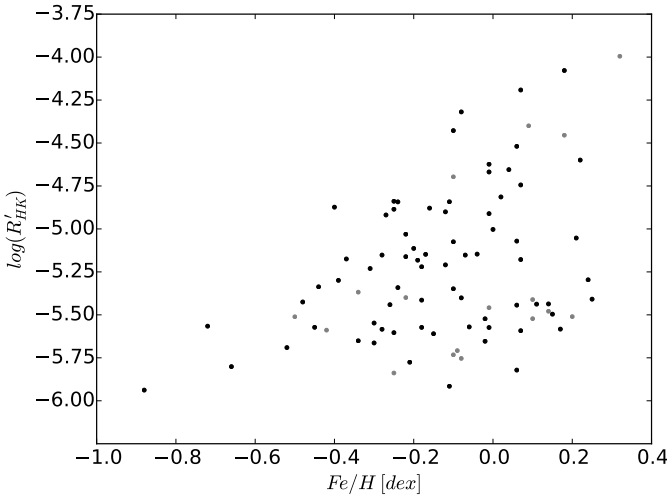


Fig. 7. $\log(R'_{HK})$ as a function of metallicity. Black dots represent stars with at least 6 spectra which have $S/N_{VR,pix} \geq 5$, while grey dots depict targets which don't match that condition. The lower envelope has no obvious trend with metallicity.

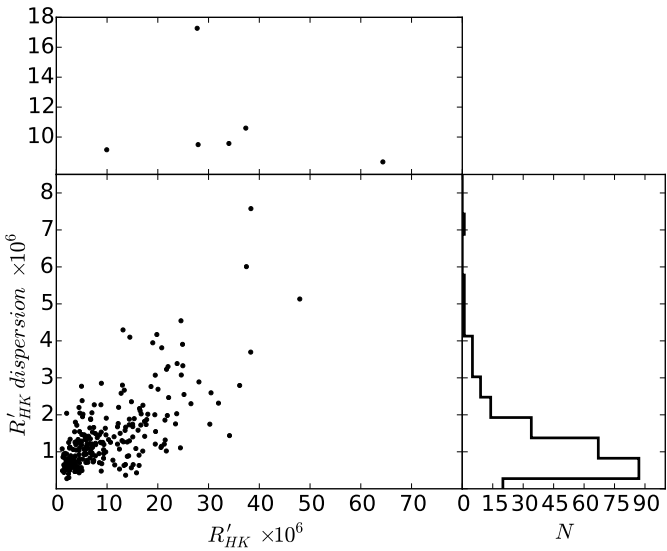


Fig. 8. Average R'_{HK} -index against the dispersion of its individual measurement for the 248 M-dwarfs which satisfy the selection criteria described in the text. For clarity, the upper and lower panels separately display the most variable stars and the bulk of the distribution with different scales. The right-side panel shows a histogram of the R'_{HK} dispersion.

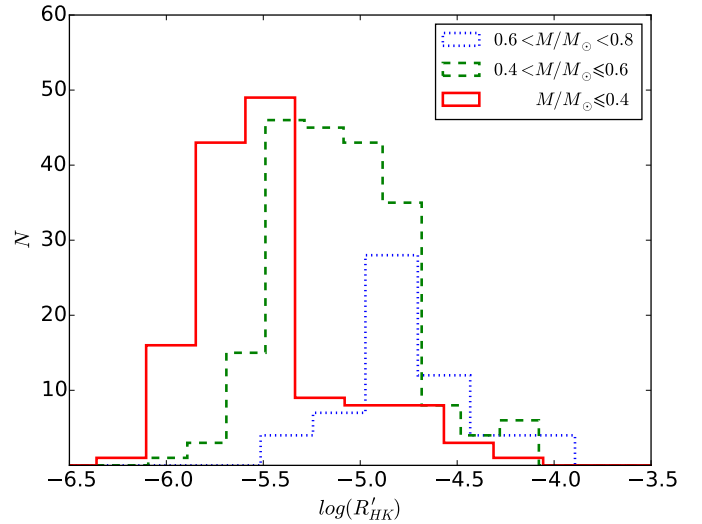


Fig. 9. Histograms of the median $\log(R'_{HK})$ for three non-overlapping M-dwarf mass bins. The 403 M-dwarfs used in the histograms divide into 138 that are less massive than $0.4M_{\odot}$, 206 with masses between $0.4M_{\odot}$ and $0.6M_{\odot}$, and 59 above $0.6M_{\odot}$. Less massive M-dwarfs are, on average, less active.

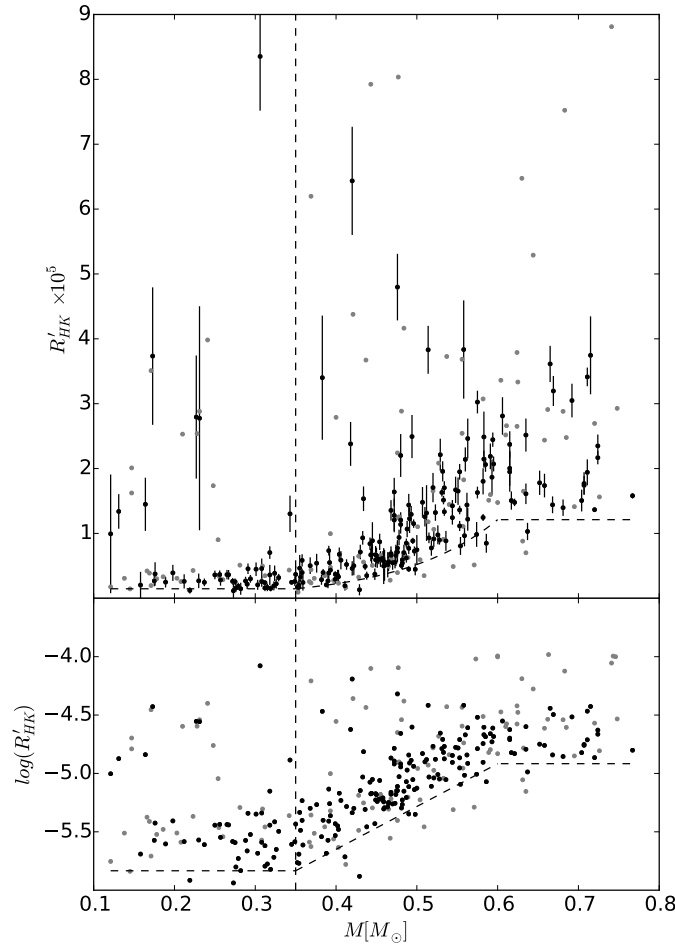


Fig. 10. Median R'_{HK} as a function of stellar mass, with the vertical errorbar representing the dispersion of the individual measurements (upper panel). $\log(R'_{HK})$ as a function of stellar mass (lower panel). Black dots represent targets with at least six measurements with $S/N_{VR,pix} > 5$, while grey dots represent the rest of the stars. Activity decreases with stellar mass down to approximately the mass for full convection ($0.35 M_\odot$, marked by the vertical dashed line). Interestingly, M-dwarfs departing further from the lower envelope (dashed curve) are those which present higher variability.

Table A.2. C_{cf} and median R_{phot} for standards. C_{cf} values are derived from Middelkoop (1982)'s relation. R_{phot} is obtained in the same way as is described in table A.1.

Name	B-V	I-K	V-K	BC_v	$\log C_{cf}$	$\log(R_{phot})$	Name	B-V	I-K	V-K	BC_v	$\log C_{cf}$	$\log(R_{phot})$
BD-013125	1.24	—	—	-0.671	-0.813	—	HD 20868	1.04	—	—	-0.422	-0.469	—
BD-044138	1.19	—	—	-0.601	-0.723	—	HD 208704	0.64	—	1.475	-0.085	0.042	-4.413
HD 10180	0.63	—	1.438	-0.079	0.050	-4.395	HD 209449	0.72	—	—	-0.138	-0.028	—
HD 10700	0.72	0.730	—	-0.139	-0.03	-4.527	HD 210752	0.54	—	1.364	-0.03	0.101	-4.288
HD 109271	0.66	—	—	-0.097	0.028	—	HD 210918	0.65	—	1.544	-0.091	0.034	-4.462
HD 114613	0.70	0.650	—	-0.124	-0.01	-4.492	HD 211038	0.89	—	—	-0.277	-0.243	—
HD 114747	0.92	—	2.013	-0.304	-0.287	-4.674	HD 212708	0.73	—	—	-0.146	-0.041	—
HD 11505	0.64	—	1.521	-0.085	0.042	-4.431	HD 213042	1.08	—	2.511	-0.471	-0.54	-4.896
HD 115617	0.71	—	—	-0.132	-0.02	-4.532	HD 213240	0.60	—	1.432	-0.063	0.069	—
HD 123180	1.02	—	—	-0.406	-0.447	—	HD 213575	0.67	—	1.609	-0.104	0.017	-4.549
HD 124364	0.67	—	1.627	-0.104	0.017	-4.493	HD 214867	0.66	—	1.535	-0.099	0.025	—
HD 124785	0.57	—	—	-0.047	0.086	—	HD 215152	0.97	—	2.311	-0.352	-0.363	-4.835
HD 125455	0.87	—	2.015	-0.259	-0.215	-4.684	HD 217221	0.94	—	—	-0.324	-0.32	—
HD 125595	1.11	—	—	-0.502	-0.585	—	HD 217395	0.58	—	—	-0.052	0.080	—
HD 125612	0.63	—	—	-0.078	0.051	—	HD 21749	1.13	—	2.681	-0.528	-0.623	-4.924
HD 126525	0.68	—	1.611	-0.111	0.009	-4.485	HD 220339	0.88	—	2.185	-0.268	-0.229	-4.805
HD 126999	1.19	—	—	-0.594	-0.715	—	HD 220456	0.63	—	—	-0.077	0.053	—
HD 127339	1.40	—	—	-0.926	-1.061	—	HD 220507	0.69	—	1.595	-0.117	-0.001	—
HD 128674	0.67	—	1.667	-0.104	0.017	-4.514	HD 221503	1.29	—	—	-0.736	-0.887	—
HD 129191	0.68	—	—	-0.112	0.007	—	HD 221580	0.69	—	—	-0.116	0.000	—
HD 129642	0.94	—	2.224	-0.322	-0.317	-4.807	HD 223121	0.94	—	2.145	-0.322	-0.317	-4.644
HD 132569	0.89	—	—	-0.277	-0.243	—	HD 223171	0.66	—	1.511	-0.098	0.026	-4.497
HD 134060	0.62	—	1.430	-0.073	0.057	—	HD 224063	0.73	—	—	-0.149	-0.045	—
HD 134088	0.60	—	—	-0.06	0.072	—	HD 24633	0.83	—	—	-0.223	-0.158	—
HD 134440	0.88	0.970	2.260	-0.268	-0.229	—	HD 27063	0.67	—	1.524	-0.104	0.017	-4.446
HD 134664	0.66	—	1.488	-0.098	0.026	-4.435	HD 28821	0.68	—	1.589	-0.111	0.009	-4.49
HD 135625	0.62	—	—	-0.071	0.059	—	HD 290327	0.76	—	—	-0.169	-0.075	—
HD 136352	0.65	—	—	-0.091	0.034	-4.44	HD 30177	0.77	—	—	-0.178	-0.089	—
HD 136713	0.97	—	2.223	-0.352	-0.363	-4.792	HD 31527	0.61	—	1.417	-0.067	0.064	-4.369
HD 13808	0.87	—	2.086	-0.259	-0.215	-4.725	HD 31822	0.58	—	1.315	-0.05	0.082	—
HD 144411	0.98	—	2.379	-0.361	-0.378	-4.843	HD 3220	0.60	—	—	-0.062	0.069	—
HD 144585	0.66	—	1.496	-0.098	0.026	-4.445	HD 323631	0.93	—	—	-0.313	-0.302	—
HD 144628	0.86	—	2.105	-0.25	-0.201	-4.764	HD 323684	1.27	—	—	-0.703	-0.85	—
HD 145377	0.62	—	—	-0.075	0.055	—	HD 330075	0.94	—	2.165	-0.317	-0.309	-4.738
HD 1461	0.67	—	1.549	-0.104	0.017	-4.462	HD 36003	1.11	—	2.746	-0.505	-0.59	-5.013
HD 146233	0.65	—	—	-0.091	0.034	-4.455	HD 36379	0.56	—	1.362	-0.039	0.093	—
HD 147512	0.72	—	1.694	-0.139	-0.03	-4.542	HD 3823	0.56	—	—	-0.039	0.093	—
HD 147642	0.57	—	—	-0.046	0.087	—	HD 38973	0.59	—	1.386	-0.055	0.077	—
HD 147935	0.73	—	—	-0.148	-0.044	—	HD 40307	0.94	—	2.353	-0.322	-0.317	-4.916
HD 148211	0.55	—	—	-0.036	0.096	—	HD 40865	0.63	—	—	-0.077	0.053	—
HD 148303	0.98	—	2.315	-0.361	-0.378	-4.836	HD 44420	0.69	—	1.508	-0.117	-0.001	-4.426
HD 148577	0.66	—	—	-0.10	0.023	—	HD 44573	0.92	—	2.181	-0.304	-0.287	-4.77
HD 149396	0.70	—	—	-0.127	-0.014	—	HD 45184	0.62	—	1.495	-0.073	0.057	-4.434
HD 153950	0.56	—	—	-0.042	0.090	—	HD 457	0.62	—	—	-0.073	0.057	—
HD 154577	0.89	—	2.265	-0.277	-0.243	-4.872	HD 47186	0.71	—	1.601	-0.132	-0.02	-4.486
HD 156411	0.61	—	—	-0.069	0.061	—	HD 4915	0.66	—	1.607	-0.098	0.026	-4.498
HD 157338	0.59	—	1.402	-0.055	0.077	—	HD 52919	1.08	—	2.601	-0.471	-0.54	-4.949
HD 160691	0.69	—	—	-0.12	-0.005	-4.504	HD 564	0.59	—	—	-0.058	0.074	—
HD 16280	1.06	—	—	-0.448	-0.507	—	HD 59468	0.69	—	1.654	-0.117	-0.001	-4.502
HD 163436	0.92	—	—	-0.303	-0.285	—	HD 69830	0.75	—	—	-0.161	-0.063	-4.569
HD 166724	0.86	—	2.060	-0.25	-0.201	-4.711	HD 7134	0.59	—	1.417	-0.055	0.077	-4.36
HD 16714	0.71	—	1.689	-0.132	-0.02	-4.524	HD 71835	0.77	—	1.740	-0.176	-0.086	-4.549
HD 171028	0.61	—	—	-0.067	0.064	—	HD 8326	0.97	—	2.232	-0.352	-0.363	-4.758
HD 172513	0.75	—	1.694	-0.161	-0.063	-4.544	HD 8638	0.68	—	1.649	-0.111	0.009	-4.484
HD 181433	1.01	—	2.282	-0.392	-0.426	-4.797	HD 92588	0.88	—	—	-0.268	-0.229	-4.764
HD 188559	1.05	—	2.448	-0.437	-0.491	-4.846	HD 9578	0.61	—	—	-0.068	0.063	—
HD 191797	0.91	—	—	-0.291	-0.266	—	HD 967	0.65	—	1.614	-0.091	0.034	-4.45
HD 192310	0.88	—	—	-0.268	-0.229	-4.727	HD 96700	0.61	—	1.491	-0.067	0.064	-4.416
HD 199960	0.64	—	1.415	-0.085	0.042	—	HIP 102964	1.01	—	—	-0.392	-0.426	—
HD 200538	0.61	—	—	-0.065	0.067	—	HIP 107758	1.37	—	—	-0.86	-1.008	—
HD 202206	0.71	—	1.571	-0.135	-0.024	-4.444	HIP 117865	1.10	—	—	-0.492	-0.57	—
HD 202871	0.56	—	—	-0.04	0.092	—	HIP 5158	1.08	—	—	-0.469	-0.537	—
HD 20794	0.71	0.720	—	-0.132	-0.02	-4.516	HD 207129	0.60	—	—	-0.061	0.070	-4.353

Table A.3. The Ca II H&K analysis for the HARPS M-dwarf sample. We listed: **i)** The V magnitude, B-V, V-K color-indexes and their references (Ref. Phot., see below). **ii)** The parallax (π), its uncertainty (σ_π) and the references (Ref. π , see below). **iii)** The stellar masses. **iv)** The number of spectra used in the analysis for a given target (N). **vi)** The median of the S-index and its dispersion (σ_S); **vii)** The median of the R'_{HK} and its dispersion ($\sigma_{R'_{HK}}$). **viii)** The rotation period derived from Eq. (12). **ix)** The averaged S/N in the violet and red bands. References: (1) : Leggett (1992); (2) : Gaidos et al. (2014); (3) : van Leeuwen (2007); (4) : van Altena et al. (1995); (5) : RECONS; (6) : Lépine & Gaidos (2011).

Name	V	B-V	V-K	π	σ_π	Ref. Phot, π	M	N	S	σ_S	$\log(R'_{HK})$	$\sigma_{R'_{HK}} \times 10^5$	P_{rot} [d]	S/N_{VR}
				[mas]	[mas]		M/M_\odot							
Gl551	11.09	1.90	6.730	771.64	2.60	(1),(3)	0.12	76	11.265	9.641	-5.003	0.915	42	7.5
Gl388	9.32	1.53	4.710	204.60	2.80	(1),(3)	0.42	41	8.690	1.089	-4.191	0.834	12	28.3
LHS3746	11.82	1.54	5.078	134.29	1.31	(2),(5)	0.24	6	0.783	0.109	-5.610	0.058	107	7.2
HIP74261	10.73	1.28	3.558	41.26	2.31	(2),(3)	0.60	5	1.685	0.079	-4.473	0.182	19	12.4
HD329868	10.81	1.21	3.698	46.39	3.65	(2),(3)	0.56	6	1.452	0.154	-4.609	0.308	23	10.4
HD329879	11.25	1.34	3.731	36.84	2.45	(2),(3)	0.58	12	1.506	0.202	-4.604	0.391	23	10.1
LHS1134	13.05	1.59	5.316	113.90	34.20	(2),(3)	0.17	4	0.665	0.452	-5.733	0.034	129	3.2
GJ163	11.82	1.52	4.680	66.69	1.82	(1),(3)	0.40	179	0.703	0.135	-5.480	0.106	87	9.4
HIP19394	11.90	1.37	4.741	66.69	1.82	(2),(3)	0.40	20	0.684	0.094	-5.532	0.070	95	9.3
BD-120662	10.12	1.25	3.648	45.28	1.97	(2),(3)	0.71	8	1.846	0.069	-4.467	0.144	19	17.4
BD-120525	10.92	1.24	3.672	33.76	1.88	(2),(3)	0.68	3	1.626	0.110	-4.540	0.225	21	8.4
BD-090956	10.41	1.33	4.115	50.80	3.74	(2),(3)	0.69	5	1.292	0.084	-4.850	0.113	33	11.2
BD-126174	10.27	1.23	3.848	45.00	2.68	(2),(3)	0.72	21	1.583	0.101	-4.629	0.175	24	15.2
Gl832	8.66	1.50	4.180	201.87	1.01	(1),(3)	0.45	62	0.765	0.097	-5.182	0.122	55	38.0
Gl887	7.34	1.50	3.960	305.26	0.70	(1),(3)	0.49	76	1.155	0.111	-4.843	0.173	33	48.3
LTT9759	10.34	1.09	4.767	100.07	1.05	(2),(3)	0.54	11	1.512	0.211	-5.053	0.153	46	14.4
GJ1001	12.85	1.62	5.089	76.86	3.97	(2),(5)	0.26	15	0.867	0.156	-5.542	0.083	96	4.1
Gl1	8.55	1.48	4.030	230.42	0.90	(1),(3)	0.39	48	0.419	0.077	-5.572	0.112	101	44.0
L225-57	12.61	1.53	5.275	97.00	29.10	(2),(3)	0.25	11	0.687	0.146	-5.829	0.065	149	5.6
Gl145	11.59	1.44	4.659	93.11	1.94	(2),(3)	0.32	7	1.158	0.121	-5.152	0.097	53	10.0
GJ1061	13.06	1.83	6.426	271.92	1.34	(2),(5)	0.12	6	1.963	0.337	-5.754	0.045	133	3.1
Gl191	8.84	1.56	3.790	255.66	0.91	(1),(3)	0.27	31	0.286	0.060	-5.938	0.108	176	38.8
HIP31293	10.60	1.36	4.714	110.88	2.25	(2),(3)	0.43	9	1.222	0.147	-5.147	0.112	53	14.2
HIP31292	11.50	1.51	4.918	115.19	10.61	(2),(3)	0.30	19	1.021	0.166	-5.348	0.104	72	7.3
Gl358	10.72	1.49	4.660	105.63	1.64	(1),(3)	0.42	37	3.246	0.422	-4.623	0.339	24	16.4
Gl367	10.29	1.33	4.486	101.31	3.18	(2),(3)	0.48	25	1.010	0.128	-5.152	0.121	53	22.1
Gl1123	13.16	1.61	5.688	110.92	2.02	(2),(5)	0.20	5	1.477	0.320	-5.510	0.094	92	2.4
Gl803	8.81	1.45	4.230	100.91	1.06	(1),(3)	0.74	4	8.637	0.323	-3.995	0.389	10	32.1
LHS3583	11.60	1.52	4.750	94.72	2.38	(2),(5)	0.32	6	0.812	0.162	-5.414	0.119	79	6.4
Gl908	8.98	1.47	3.930	167.29	1.23	(1),(3)	0.42	89	0.518	0.069	-5.337	0.111	70	36.8
Gl54.1	12.16	1.74	5.716	271.01	8.36	(2),(3)	0.13	15	5.115	0.933	-4.873	0.267	35	5.9
Gl105B	11.66	1.61	5.050	137.00	27.40	(1),(3)	0.25	21	0.715	0.253	-5.654	0.062	114	9.1
GJ1057	13.79	1.82	5.950	105.80	5.10	(1),(2)	0.18	6	1.828	0.501	-5.522	0.113	93	3.1
GJ1065	12.87	1.65	5.095	105.40	21.10	(2),(2)	0.18	6	0.914	0.406	-5.399	0.146	77	4.2
Gl176	10.14	1.35	4.509	107.83	2.85	(2),(3)	0.49	71	1.593	0.238	-4.911	0.220	37	20.8
LHS1723	12.22	1.70	5.460	187.92	1.26	(2),(5)	0.16	7	4.298	1.108	-4.839	0.410	33	5.4
Gl205	7.95	1.47	4.080	176.77	1.18	(1),(3)	0.64	103	2.050	0.184	-4.599	0.255	23	43.9
Gl213	11.53	1.64	5.160	171.55	3.99	(1),(3)	0.22	18	0.571	0.123	-5.915	0.049	170	8.3
Gl229	8.12	1.50	3.970	173.81	0.99	(1),(3)	0.58	24	1.624	0.086	-4.669	0.132	25	57.6
Gl250B	10.25	1.31	4.503	114.80	0.40	(2),(2)	0.44	12	1.171	0.102	-5.075	0.095	47	19.5
Gl273	9.86	1.57	4.980	262.98	1.39	(1),(3)	0.29	98	0.765	0.110	-5.574	0.065	101	24.4
Gl285	11.15	1.61	5.420	167.88	2.31	(1),(3)	0.31	7	22.068	2.173	-4.078	0.837	10	7.8
Gl299	12.83	1.72	5.190	148.70	6.00	(1),(2)	0.14	21	0.880	0.419	-5.511	0.163	92	3.4
Gl300	12.19	1.62	5.461	125.60	0.97	(2),(5)	0.26	39	1.374	0.171	-5.436	0.063	82	9.1
Gl357	11.02	1.50	4.521	110.82	1.92	(2),(3)	0.33	51	0.510	0.127	-5.651	0.073	114	13.4
Gl382	9.26	1.50	4.170	127.08	1.90	(1),(3)	0.53	33	1.979	0.193	-4.655	0.247	25	29.5
Gl393	9.65	1.51	4.310	141.50	2.22	(1),(3)	0.43	29	1.087	0.094	-5.031	0.106	44	28.9
Gl876	10.18	1.58	5.120	213.28	2.12	(1),(3)	0.33	184	0.949	0.111	-5.496	0.057	90	18.9
Gl12	12.64	1.63	4.809	85.85	2.57	(2),(5)	0.22	5	0.911	0.229	-5.368	0.160	74	4.7
Gl83.1	12.41	1.72	5.738	217.70	8.60	(2),(2)	0.15	25	6.244	1.516	-4.790	0.424	30	4.8
LHS1610	13.86	1.70	5.783	101.57	2.07	(2),(5)	0.17	2	2.028	0.170	-5.375	0.045	75	2.5
LHS1731	11.83	1.54	4.870	108.61	2.66	(2),(3)	0.27	9	0.853	0.112	-5.441	0.074	82	7.8
Gl203	12.49	1.55	4.924	113.50	5.01	(2),(3)	0.19	10	0.698	0.251	-5.604	0.083	106	5.2
G108-21	12.12	1.53	4.762	77.90	2.80	(2),(2)	0.31	4	0.768	0.096	-5.458	0.070	85	7.4
LHS1935	11.80	1.53	4.713	94.31	3.31	(2),(3)	0.29	8	0.883	0.106	-5.342	0.081	71	7.7
GJ2066	10.23	1.42	4.440	109.62	1.54	(2),(3)	0.45	8	0.872	0.078	-5.220	0.077	59	21.5
Gl87	10.04	1.45	3.990	96.02	1.66	(1),(3)	0.46	25	0.622	0.062	-5.230	0.094	60	21.0
LHS1481	12.71	1.71	4.487	95.50	10.90	(2),(2)	0.17	8	0.525	0.328	-5.566	0.134	100	5.1
GJ1125	11.80	1.46	4.905	103.46	3.94	(2),(3)	0.29	9	0.647	0.116	-5.664	0.074	116	10.2
GJ1129	12.50	1.60	5.219	90.93	3.78	(2),(5)	0.28	6	0.890	0.108	-5.592	0.050	104	5.1
Gl402	11.65	1.65	5.230	147.92	3.52	(1),(3)	0.25	6	1.123	0.143	-5.443	0.067	83	8.9
Gl880	8.66	1.49	4.130	146.09	1.00	(1),(3)	0.58	27	1.602	0.152	-4.744	0.202	28	32.1

Table A.3. continued.

Name	V	B-V	V-K	π	σ_π	Ref.	M	N	S	σ_S	$\log(R'_{HK})$	$\sigma_{R'_{HK}} \times 10^5$	P_{rot}	S/N_{VR}
				[mas]	[mas]	Phot./ π	M/M $_\odot$							
LHS543	11.77	1.41	5.239	91.00	2.89	(2),(3)	0.39	7	1.196	0.228	-5.409	0.105	78	9.2
HIP38594	9.89	1.21	3.697	51.52	1.46	(2),(3)	0.71	17	1.190	0.100	-4.712	0.200	27	16.5
Gl433	9.82	1.51	4.200	112.58	1.44	(1),(3)	0.47	86	0.819	0.074	-5.148	0.091	53	23.4
Gl849	10.38	1.50	4.740	109.94	2.07	(1),(3)	0.48	51	0.968	0.066	-5.296	0.049	66	19.8
GJ1265	13.67	1.73	5.531	96.00	3.90	(2),(2)	0.17	5	0.964	0.184	-5.708	0.063	124	2.8
LHS3799	13.31	1.80	5.967	138.17	1.87	(2),(5)	0.17	2	16.407	3.145	-4.455	0.694	18	2.6
HIP6097	11.87	1.40	4.296	45.20	3.50	(2),(3)	0.48	6	1.257	0.124	-4.944	0.141	39	7.3
HIP12961	10.38	1.27	3.620	43.45	1.72	(2),(3)	0.67	46	1.701	0.108	-4.495	0.232	19	18.1
HIP31148	11.49	1.25	3.672	37.57	2.29	(2),(3)	0.51	6	0.860	0.210	-4.881	0.430	35	12.5
HIP34785	10.51	1.19	3.596	37.47	1.93	(2),(3)	0.70	15	0.899	0.076	-4.822	0.168	32	18.8
BD-082582	9.57	0.90	3.789	68.69	1.29	(2),(3)	0.67	18	2.196	0.153	-4.442	0.279	18	16.9
HIP48502	10.30	1.24	3.708	41.45	1.55	(2),(3)	0.73	1	1.010	0.000	-4.806	0.000	31	12.9
HD304043	11.67	1.39	4.611	78.91	2.60	(2),(3)	0.35	18	0.519	0.112	-5.692	0.094	121	10.2
HIP27323	9.9	1.16	3.582	48.18	0.98	(2),(3)	0.71	10	1.892	0.269	-4.426	0.601	18	13.8
BD-093070	10.32	1.33	4.264	81.00	1.91	(2),(3)	0.53	6	1.647	0.054	-4.788	0.063	30	19.2
Gl514	9.05	1.49	3.990	130.62	1.05	(1),(3)	0.52	16	1.107	0.084	-4.879	0.127	35	36.1
Gl555	11.31	1.63	5.300	164.99	3.29	(1),(3)	0.27	14	0.960	0.115	-5.583	0.050	102	11.1
LHS3056	12.90	1.49	5.294	79.60	23.90	(2),(3)	0.27	6	1.223	0.194	-5.422	0.085	80	4.9
Gl581	10.56	1.60	4.710	154.66	2.62	(1),(5)	0.32	247	0.505	0.078	-5.776	0.057	137	16.2
Gl588	9.31	1.53	4.530	168.66	1.30	(1),(3)	0.47	42	1.001	0.091	-5.178	0.083	55	33.3
Gl846	9.17	1.47	3.730	97.61	1.53	(1),(3)	0.57	55	1.782	0.090	-4.519	0.175	20	28.4
GJ1256	13.34	1.83	5.567	114.50	3.20	(2),(2)	0.17	5	1.570	0.731	-5.411	0.243	79	2.5
LP816-60	11.60	1.55	5.377	175.03	3.40	(2),(3)	0.23	7	1.039	0.279	-5.570	0.112	100	10.1
Gl479	10.66	1.55	4.640	103.18	2.31	(1),(3)	0.43	58	2.155	0.232	-4.814	0.190	32	19.8
LHS337	12.78	1.68	5.370	156.78	1.99	(2),(5)	0.14	7	0.663	0.291	-5.838	0.068	151	4.6
Gl480.1	12.29	1.65	4.853	128.52	3.90	(2),(3)	0.18	10	0.863	0.270	-5.425	0.180	80	5.3
Gl526	8.47	1.43	4.010	185.49	1.10	(1),(3)	0.49	34	0.753	0.060	-5.113	0.089	50	43.7
Gl536	9.87	1.25	4.163	99.72	1.57	(2),(3)	0.51	20	1.222	0.117	-4.901	0.150	36	26.5
Gl569A	10.21	1.38	4.416	103.59	1.72	(2),(3)	0.48	23	5.004	0.507	-4.319	0.513	15	15.4
Gl628	10.08	1.58	4.980	232.98	1.60	(1),(3)	0.29	44	0.821	0.101	-5.523	0.060	93	22.7
Gl618A	10.66	1.47	4.686	119.85	2.52	(2),(3)	0.38	20	0.790	0.069	-5.401	0.054	78	18.1
Gl643	11.77	1.69	5.030	148.92	4.00	(1),(3)	0.21	10	0.783	0.195	-5.584	0.110	102	7.1
Gl674	9.38	1.53	4.480	220.24	1.42	(1),(3)	0.34	48	1.633	0.294	-4.885	0.280	35	32.0
Gl682	10.95	1.65	5.270	196.90	2.15	(1),(3)	0.27	21	1.170	0.163	-5.438	0.073	82	12.0
Gl693	10.86	1.52	4.820	171.48	2.31	(2),(3)	0.26	12	0.708	0.129	-5.548	0.089	97	11.6
Gl701	9.37	1.50	4.030	128.89	1.43	(1),(3)	0.47	31	1.063	0.115	-4.919	0.168	37	27.0
GJ1224	13.90	1.16	6.049	126.54	1.05	(2),(5)	0.15	5	10.455	5.401	-4.697	1.093	26	2.3
G141-29	12.81	1.58	5.235	90.09	1.91	(2),(5)	0.24	4	8.967	3.392	-4.400	1.567	17	2.7
Gl729	10.47	1.72	5.080	336.72	2.03	(1),(3)	0.17	8	7.278	1.973	-4.428	1.060	18	12.5
GJ1232	13.31	1.01	5.384	97.40	2.50	(2),(2)	0.19	5	1.202	0.402	-5.479	0.161	87	2.6
Gl413.1	10.59	1.34	4.469	93.00	1.69	(2),(3)	0.46	19	0.907	0.115	-5.209	0.110	58	19.7
Gl465	11.29	1.61	4.490	112.98	2.51	(1),(3)	0.28	20	0.430	0.109	-5.801	0.062	143	10.9
Gl486	11.38	1.56	5.000	119.47	2.69	(1),(3)	0.32	12	0.577	0.076	-5.821	0.044	147	9.1
Gl680	10.26	1.39	4.407	102.83	2.75	(2),(3)	0.47	38	0.936	0.109	-5.161	0.111	54	18.6
Gl678.1A	9.65	1.10	4.204	100.23	1.07	(2),(3)	0.56	32	1.410	0.152	-4.842	0.188	33	27.1
Gl686	9.62	1.53	4.040	123.67	1.61	(1),(3)	0.44	20	0.700	0.068	-5.175	0.098	55	22.5
Gl752A	9.12	1.50	4.460	170.36	1.00	(1),(3)	0.49	24	1.140	0.073	-5.071	0.071	47	37.3
GJ1236	12.46	1.60	4.748	96.90	1.30	(2),(2)	0.21	8	0.638	0.060	-5.589	0.044	103	4.0
HIP95903	11.38	1.29	3.486	28.89	2.73	(2),(3)	0.61	36	1.029	0.110	-4.698	0.269	27	9.0
HIP10688	11.48	1.31	3.805	43.61	2.54	(2),(3)	0.48	7	0.653	0.068	-5.112	0.123	50	12.0
HIP100490	10.69	1.30	3.697	51.58	1.92	(2),(3)	0.54	5	0.942	0.037	-4.840	0.074	33	15.5
BD-035691	10.45	1.19	3.569	45.24	2.05	(2),(3)	0.62	1	1.890	0.000	-4.421	0.000	17	17.0
BD-226219	10.91	1.32	3.769	41.22	2.64	(2),(3)	0.61	3	1.648	0.043	-4.575	0.080	22	14.6
Gl438	10.48	1.37	4.136	91.70	2.05	(2),(5)	0.42	19	0.588	0.230	-5.299	0.147	66	34.2
HIP85126	11.70	1.41	4.157	41.78	4.12	(2),(3)	0.52	8	0.952	0.097	-5.039	0.125	45	8.2
HD162283	10.25	1.30	3.685	45.89	2.18	(2),(3)	0.69	5	1.444	0.205	-4.606	0.414	23	18.1
HIP73194	11.55	1.25	3.690	40.81	4.60	(2),(3)	0.47	3	1.247	0.102	-4.684	0.206	26	13.3
Gl447	11.12	1.76	5.490	298.04	2.30	(1),(3)	0.17	12	1.133	0.228	-5.573	0.082	101	11.5
Gl452.1	12.88	1.61	4.984	88.30	3.70	(2),(2)	0.21	13	4.609	0.848	-4.597	0.500	23	3.6
Gl436	10.66	1.52	4.560	98.61	2.33	(1),(3)	0.44	171	0.668	0.070	-5.457	0.062	84	12.8
HIP55119	9.95	1.18	3.731	56.52	1.28	(2),(3)	0.66	5	1.724	0.238	-4.536	0.461	21	16.7
HIP57459	11.77	1.42	4.677	50.02	3.10	(2),(3)	0.53	5	1.434	0.049	-5.041	0.039	45	11.8
BD-063950	10.28	1.30	3.685	51.64	1.76	(2),(3)	0.62	5	1.530	0.131	-4.577	0.265	22	17.1
BD-074156	10.64	1.36	4.273	71.95	1.88	(2),(3)	0.52	5	1.680	0.346	-4.781	0.400	30	14.5
HIP85647	9.95	1.03	4.101	60.79	1.62	(2),(3)	0.71	43	1.519	0.104	-4.759	0.142	29	16.1
HIP114427	11.46	1.27	3.509	30.28	2.44	(2),(3)	0.58	3	1.495	0.084	-4.512	0.201	20	10.5

Table A.3. continued.

Name	V	B-V	V-K	π	σ_π	Ref.	M	N	S	σ_S	$\log(R'_{HK})$	$\sigma_{R'_{HK}} \times 10^5$	P_{rot}	S/N_{VR}
				[mas]	[mas]	Phot./ π	M/M $_\odot$						[d]	
GJ234	11.20	1.62	5.690	242.32	3.12	(2),(3)	0.23	4	10.240	0.777	-4.540	0.228	21	16.9
GJ494	9.76	1.47	4.150	85.54	1.53	(1),(3)	0.60	1	8.044	0.000	-3.994	0.000	10	28.8
GJ699	9.55	1.73	5.040	548.31	1.51	(1),(3)	0.16	102	0.687	0.366	-5.691	0.204	121	21.3
GJ7	11.76	1.44	3.880	42.65	2.65	(2),(3)	0.45	11	0.756	0.170	-5.052	0.285	46	9.6
GJ46	11.86	1.45	4.944	80.95	3.21	(2),(3)	0.37	4	0.696	0.136	-5.626	0.084	109	10.3
GJ1009	11.23	1.39	4.421	55.62	2.32	(2),(3)	0.54	12	1.677	0.089	-4.846	0.089	33	13.9
GJ1036	11.35	1.41	4.388	61.68	3.43	(2),(3)	0.47	1	0.841	0.000	-5.218	0.000	59	13.8
GJ27.1	11.53	1.38	4.112	41.69	2.80	(2),(3)	0.55	50	1.481	0.150	-4.777	0.202	30	11.3
GJ3082	11.17	1.39	4.180	60.38	1.81	(2),(3)	0.47	42	1.542	0.172	-4.785	0.217	30	9.8
GJ3110	11.24	1.31	3.814	42.82	2.36	(2),(3)	0.53	12	1.177	0.057	-4.769	0.102	30	12.8
GJ3098	11.26	1.39	4.136	55.98	1.91	(2),(3)	0.48	1	1.187	0.000	-4.905	0.000	36	13.5
GJ2003	11.72	1.45	4.001	43.11	3.75	(2),(3)	0.47	41	1.087	0.173	-4.894	0.258	36	9.3
GJ1293	10.87	1.29	3.629	31.13	2.21	(2),(3)	0.72	7	0.856	0.017	-4.865	0.037	34	17.5
GJ56.1	11.87	1.40	4.296	45.20	3.50	(2),(3)	0.48	7	1.316	0.107	-4.919	0.121	37	9.8
GJ3084	11.02	1.31	3.976	48.83	10.75	(2),(3)	0.55	5	1.181	0.049	-4.838	0.075	33	14.8
GJ3103	11.67	1.36	4.322	49.44	3.00	(2),(3)	0.49	7	0.817	0.065	-5.206	0.072	58	11.9
GJ70	10.95	1.51	4.410	87.62	2.00	(2),(3)	0.40	9	0.926	0.104	-5.169	0.106	54	15.2
GJ3138	10.98	1.29	3.710	33.44	2.17	(2),(3)	0.68	20	0.927	0.064	-4.855	0.126	34	15.1
GJ84.1A	11.02	1.21	3.832	43.03	2.08	(2),(3)	0.58	8	0.934	0.030	-4.905	0.053	36	18.7
GJ91	10.46	1.34	4.343	79.68	1.69	(2),(3)	0.53	26	1.158	0.135	-5.009	0.146	43	18.8
GJ1046	11.65	1.47	4.595	71.06	3.23	(2),(3)	0.39	7	0.784	0.088	-5.362	0.075	73	11.5
GJ1050	11.81	1.52	4.481	87.70	2.38	(2),(5)	0.28	10	0.462	0.054	-5.729	0.052	128	10.5
GJ130	11.57	1.46	4.361	79.60	9.70	(2),(5)	0.33	5	0.585	0.215	-5.379	0.063	75	28.9
GJ93	11.48	1.31	3.805	43.61	2.54	(2),(3)	0.48	11	0.619	0.085	-5.147	0.153	53	12.6
GJ114.1A	10.80	1.40	4.281	77.19	1.64	(2),(3)	0.46	47	0.746	0.137	-5.244	0.134	61	17.2
GJ118	11.49	1.46	4.637	85.87	1.99	(2),(3)	0.36	20	0.762	0.074	-5.402	0.061	78	9.6
GJ126	11.68	1.30	3.926	32.81	2.29	(2),(3)	0.59	32	0.758	0.091	-5.071	0.146	47	10.7
GJ3260	11.51	1.38	4.029	47.80	14.40	(2),(3)	0.47	6	1.921	0.312	-4.610	0.454	23	6.8
GJ173	10.49	1.36	4.375	90.10	1.74	(2),(3)	0.47	16	0.785	0.088	-5.256	0.093	62	19.5
GJ3218	11.40	1.43	4.393	53.60	16.10	(2),(3)	0.52	46	2.360	0.313	-4.663	0.323	25	12.0
GJ3256	11.32	1.45	4.346	54.60	16.40	(2),(3)	0.52	29	2.089	0.386	-4.703	0.417	27	9.6
GJ155.1	11.15	1.41	4.016	59.36	2.42	(2),(3)	0.45	12	0.625	0.072	-5.240	0.106	61	13.2
GJ3307	11.31	1.36	4.254	60.00	18.00	(2),(3)	0.46	18	1.662	0.146	-4.779	0.172	30	12.2
GJ3313	11.40	1.40	3.925	39.80	11.90	(2),(3)	0.56	6	1.552	0.075	-4.672	0.121	25	12.4
GJ3321	11.39	1.38	4.133	54.90	16.50	(2),(3)	0.46	5	1.233	0.087	-4.883	0.115	35	14.1
GJ3344	11.78	1.28	4.394	46.14	1.46	(2),(5)	0.51	1	0.597	0.000	-5.457	0.000	85	12.3
GJ180	11.02	1.42	4.398	82.52	2.40	(2),(3)	0.41	37	0.766	0.078	-5.283	0.080	65	16.0
GJ182	10.07	1.41	3.680	38.64	2.54	(1),(3)	0.80	3	7.032	0.321	-3.859	0.653	10	23.2
GJ3328	11.60	1.36	4.141	46.90	14.10	(2),(3)	0.49	8	0.985	0.076	-5.012	0.100	43	10.9
GJ3340	11.66	1.38	4.118	44.54	4.06	(2),(3)	0.49	10	1.206	0.097	-4.888	0.130	35	11.1
GJ206	11.53	1.63	4.920	78.16	3.70	(1),(3)	0.44	1	6.168	0.000	-4.435	0.000	18	11.5
GJ207.1	11.58	1.42	4.701	62.75	4.02	(2),(3)	0.48	1	10.690	0.000	-4.095	0.000	11	14.1
GJ3362	11.50	1.29	4.277	59.90	18.00	(2),(3)	0.43	2	2.327	1.546	-4.621	1.783	24	9.5
GJ3369	11.07	1.33	3.762	37.39	2.24	(2),(3)	0.62	9	1.009	0.030	-4.830	0.057	32	17.3
GJ3379	11.40	1.57	5.334	190.93	1.89	(2),(5)	0.23	16	7.027	2.264	-4.554	0.949	21	7.5
GJ218	10.74	1.46	4.080	66.54	1.43	(1),(3)	0.49	9	0.876	0.034	-5.053	0.048	46	18.2
GJ9206	11.36	1.31	3.920	35.48	2.09	(2),(3)	0.62	8	1.162	0.087	-4.822	0.140	32	13.8
GJ2049	10.86	1.24	3.872	40.00	3.15	(2),(3)	0.66	55	1.254	0.108	-4.760	0.182	29	13.9
GJ3367	11.00	1.30	3.817	47.10	14.10	(2),(3)	0.54	5	4.805	0.649	-4.088	1.157	10	8.2
GJ234A	11.20	1.62	5.690	242.32	3.12	(2),(3)	0.23	16	9.880	5.880	-4.557	1.727	21	9.5
GJ1097	11.51	1.46	4.782	81.38	2.49	(2),(3)	0.40	8	0.811	0.065	-5.431	0.047	81	11.9
GJ1135	10.13	1.28	4.113	61.21	1.52	(2),(3)	0.67	22	1.311	0.096	-4.841	0.130	33	24.1
GJ1100	11.56	1.30	3.807	34.57	2.79	(2),(3)	0.56	32	0.902	0.098	-4.914	0.176	37	11.5
GJ3440	11.84	1.44	4.268	40.80	12.30	(2),(3)	0.53	26	1.884	0.339	-4.721	0.395	27	5.0
GJ298	11.73	1.51	4.320	60.68	2.48	(1),(3)	0.39	7	0.917	0.068	-5.134	0.075	52	9.6
GJ3501A	11.27	1.29	4.067	37.95	2.70	(2),(3)	0.64	11	0.970	0.094	-4.987	0.133	41	12.3
GJ330	10.59	1.53	4.030	58.79	2.72	(1),(3)	0.57	1	0.589	0.000	-5.289	0.000	65	10.2
GJ3528	11.87	1.33	4.536	51.25	3.72	(2),(3)	0.47	13	1.002	0.182	-5.180	0.165	55	8.0
GJ3530	11.69	1.42	4.353	57.50	17.20	(2),(3)	0.43	24	0.943	0.071	-5.132	0.077	51	9.2
GJ3543	10.85	1.40	4.334	65.50	19.60	(2),(3)	0.53	81	2.156	0.349	-4.682	0.381	26	15.7
GJ3555	11.68	1.38	4.029	36.81	2.49	(2),(3)	0.56	2	1.980	0.164	-4.595	0.239	23	7.5
GJ361	10.36	1.50	4.190	88.81	1.68	(1),(3)	0.47	104	1.327	0.126	-4.868	0.158	34	16.4
GJ377	11.54	1.38	4.816	61.39	2.55	(2),(3)	0.52	11	1.417	0.172	-5.110	0.119	50	9.9
GJ386	11.12	1.33	4.644	73.30	2.62	(2),(3)	0.49	7	0.831	0.053	-5.347	0.043	71	18.5
GJ390	10.17	1.54	4.120	81.00	1.91	(1),(3)	0.53	40	1.704	0.116	-4.708	0.155	27	22.7
GJ399	11.37	1.45	4.528	60.80	3.14	(2),(3)	0.50	8	0.760	0.102	-5.350	0.092	72	11.5

Table A.3. continued.

Name	V	B-V	V-K	π [mas]	σ_π [mas]	Ref. Phot./ π	M M/M _⊕	N	S	σ_S	$\log(R'_{HK})$	$\sigma_{R'_{HK}}$ $\times 10^5$	P_{rot} [d]	S/N_{VR}
GJ401A	11.14	1.37	3.864	49.95	2.26	(2),(3)	0.50	7	0.902	0.038	-4.939	0.064	38	17.3
GJ422	11.67	1.39	4.611	78.91	2.60	(2),(3)	0.35	19	0.476	0.124	-5.769	0.096	136	8.7
GJ2085	11.28	1.38	4.095	46.81	2.39	(2),(3)	0.54	8	1.147	0.078	-4.905	0.107	36	10.3
GJ443	11.69	1.50	4.570	50.02	3.10	(1),(3)	0.53	12	1.298	0.078	-5.048	0.068	45	10.5
GJ452A	11.95	1.44	4.481	51.10	3.58	(2),(3)	0.45	9	0.889	0.120	-5.227	0.114	59	8.5
GJ9381	11.57	1.35	4.203	38.05	2.85	(2),(3)	0.60	2	1.440	0.145	-4.831	0.179	32	9.4
GJ3695	11.90	1.37	4.302	41.35	2.81	(2),(3)	0.51	2	1.299	0.012	-4.928	0.013	38	8.3
GJ3671	11.25	1.42	3.970	56.38	2.04	(2),(3)	0.44	7	0.671	0.123	-5.170	0.189	55	10.2
GJ3708A	11.77	1.51	4.702	79.43	2.36	(2),(3)	0.35	24	0.760	0.197	-5.434	0.126	82	9.2
GJ476	11.41	1.43	4.260	54.69	3.05	(1),(3)	0.48	12	0.755	0.113	-5.227	0.132	59	11.9
GJ3778	12.05	1.41	4.350	48.60	14.60	(2),(3)	0.43	19	0.908	0.191	-5.154	0.206	53	6.3
GJ513	12.12	1.44	4.570	62.90	12.60	(1),(3)	0.35	8	0.692	0.053	-5.436	0.047	82	8.7
GJ508.3	11.89	1.32	3.813	27.96	3.61	(2),(3)	0.59	9	0.720	0.070	-5.052	0.124	46	9.6
GJ510	11.08	1.43	4.180	59.72	2.43	(2),(3)	0.49	13	2.217	0.263	-4.603	0.333	23	11.6
GJ3823	12.24	1.60	4.376	64.20	19.30	(2),(3)	0.30	3	1.454	0.089	-4.901	0.093	36	5.2
GJ618.4	11.89	1.37	4.229	41.77	3.59	(2),(3)	0.50	8	0.850	0.060	-5.139	0.073	52	8.4
GJ606	10.64	1.36	4.273	71.95	1.88	(2),(3)	0.52	18	1.725	0.195	-4.768	0.226	30	16.2
GJ618.1	10.80	1.27	3.695	29.92	2.69	(2),(3)	0.77	8	1.008	0.022	-4.801	0.043	31	14.5
GJ620	10.22	1.47	3.840	60.83	2.06	(1),(3)	0.59	22	1.628	0.063	-4.612	0.111	23	18.6
GJ724	10.75	1.34	4.180	61.15	2.07	(2),(3)	0.55	26	1.551	0.167	-4.782	0.211	30	14.4
GJ431	11.51	1.55	4.980	96.56	2.39	(1),(3)	0.37	4	0.645	0.107	-4.208	1.103	13	6.2
GJ477	11.20	1.37	4.332	52.67	3.05	(2),(3)	0.56	2	1.267	0.015	-4.955	0.016	39	10.6
GJ3759	11.01	1.37	4.052	58.94	2.40	(2),(3)	0.49	12	0.986	0.088	-4.971	0.126	40	10.6
GJ480	11.50	1.48	4.810	69.59	2.79	(1),(3)	0.47	37	1.083	0.155	-5.261	0.108	63	9.0
GJ494	9.76	1.47	4.150	85.54	1.53	(1),(3)	0.60	1	7.901	0.000	-4.002	0.000	10	16.1
GJ3799	12.14	1.41	4.135	30.00	9.00	(2),(3)	0.57	3	2.012	0.129	-4.632	0.170	24	6.7
GJ3804	11.94	1.49	5.014	97.62	5.03	(2),(3)	0.30	18	0.680	0.134	-5.684	0.077	119	8.2
GJ3813	11.73	1.41	4.562	71.00	21.30	(2),(3)	0.37	18	1.528	0.194	-4.956	0.171	39	4.8
GJ3822	10.76	1.31	4.030	50.36	2.04	(2),(3)	0.61	64	2.165	0.198	-4.551	0.289	21	11.5
GJ637	11.37	1.41	4.122	62.97	1.99	(2),(3)	0.41	17	0.681	0.105	-5.231	0.141	60	7.0
GJ634	11.65	1.45	4.292	57.40	6.60	(2),(2)	0.42	43	0.659	0.112	-5.334	0.127	70	8.7
GJ3707	12.14	1.51	5.253	77.93	2.41	(2),(5)	0.39	8	0.806	0.061	-5.684	0.027	119	9.0
GJ469	12.16	1.50	5.180	75.85	3.99	(2),(3)	0.38	10	0.929	0.161	-5.542	0.079	96	7.1
GJ3846	12.31	1.55	4.696	70.03	4.89	(2),(3)	0.31	6	0.875	0.199	-5.339	0.155	71	5.5
GJ3838	11.63	1.36	4.327	60.50	18.20	(2),(3)	0.41	6	1.526	0.080	-4.854	0.088	34	8.1
GJ552	10.66	1.49	4.250	71.39	2.10	(1),(3)	0.52	8	1.037	0.070	-5.031	0.082	44	13.3
GJ3871	11.65	1.38	4.511	80.90	24.30	(2),(3)	0.33	33	1.895	0.189	-4.823	0.175	32	7.3
GJ3874	11.34	1.27	3.928	40.78	2.48	(2),(3)	0.56	23	0.832	0.102	-5.015	0.164	43	10.9
GJ553.1	12.00	1.53	5.015	92.44	3.94	(2),(3)	0.31	9	0.599	0.089	-5.794	0.051	141	8.3
GJ570B	8.09	1.48	4.160	168.77	21.54	(1),(3)	0.64	2	1.458	0.128	-4.806	0.165	31	43.3
GJ676A	9.95	1.03	4.101	60.79	1.62	(2),(3)	0.71	80	1.539	0.128	-4.752	0.174	29	20.2
GJ4079	10.86	1.36	4.132	61.75	2.07	(2),(3)	0.51	15	3.138	0.279	-4.417	0.370	17	10.8
GJ3915	11.73	1.37	4.141	55.40	16.60	(2),(3)	0.40	20	0.913	0.173	-5.056	0.227	46	8.4
GJ3885	12.32	1.50	4.864	48.00	14.40	(2),(3)	0.48	12	0.951	0.202	-5.367	0.133	74	5.6
GJ3892	11.56	1.39	4.678	69.19	2.60	(2),(3)	0.44	9	0.905	0.072	-5.308	0.057	67	9.9
GJ3916	11.35	1.46	4.583	66.21	3.18	(2),(3)	0.48	3	0.732	0.108	-5.403	0.094	78	10.1
GJ611.3	11.69	1.30	4.101	28.17	7.39	(2),(3)	0.69	7	1.391	0.080	-4.805	0.109	31	7.2
GJ1203	12.22	1.35	4.521	59.63	3.55	(2),(3)	0.35	6	0.553	0.078	-5.585	0.071	103	7.2
GJ3962	11.60	1.34	3.885	28.12	3.55	(2),(3)	0.67	27	1.816	0.138	-4.576	0.230	22	7.9
GJ644A	9.34	1.25	4.913	161.41	5.64	(2),(3)	0.56	1	3.202	0.000	-4.738	0.000	28	23.9
GJ3973	10.99	1.37	4.192	54.86	2.18	(2),(3)	0.55	7	1.335	0.053	-4.866	0.066	34	14.9
GJ3998	10.95	1.40	4.110	56.20	2.26	(2),(3)	0.53	6	1.362	0.048	-4.820	0.065	32	12.2
GJ2128	11.56	1.48	4.430	67.08	2.69	(2),(3)	0.40	6	0.618	0.085	-5.449	0.084	83	8.8
GJ4001	10.70	1.29	3.961	51.86	2.49	(2),(3)	0.59	19	1.639	0.127	-4.660	0.198	25	12.8
GJ654	10.08	1.45	4.120	94.59	1.85	(1),(3)	0.48	18	0.646	0.070	-5.266	0.093	63	23.0
GJ3987	10.95	1.37	3.981	52.83	1.98	(2),(3)	0.53	7	1.107	0.041	-4.875	0.063	35	13.6
GJ4254	10.27	1.23	3.848	45.00	2.68	(2),(3)	0.72	10	1.468	0.402	-4.664	0.102	25	22.6
GJ855	10.82	1.33	4.066	52.22	2.17	(2),(3)	0.58	30	1.702	0.079	-4.686	0.112	26	13.1
GJ863	10.37	1.51	3.990	78.68	2.69	(1),(3)	0.48	5	1.063	0.060	-4.901	0.090	36	18.3
GJ800A	10.82	1.32	4.057	55.72	2.38	(2),(3)	0.55	28	1.023	0.054	-4.953	0.077	39	16.5
GJ821	10.87	1.54	3.930	82.18	2.17	(1),(3)	0.36	11	0.383	0.078	-5.613	0.125	107	12.8
GJ1264	9.96	1.10	4.288	61.29	1.54	(2),(3)	0.74	1	7.972	0.000	-4.055	0.000	10	12.9
GJ4206	10.76	1.34	4.094	47.06	2.55	(2),(3)	0.65	23	1.538	0.136	-4.749	0.187	29	13.3
GJ841A	10.67	1.28	4.769	62.61	2.92	(2),(3)	0.68	1	10.685	0.000	-4.124	0.000	11	12.3
GJ867A	9.54	0.97	4.716	115.01	1.32	(2),(3)	0.63	1	8.790	0.000	-4.189	0.000	12	33.0
GJ842	9.97	1.21	4.189	83.43	1.77	(2),(3)	0.57	8	1.546	0.073	-4.788	0.091	30	23.4

Table A.3. continued.

Name	V	B-V	V-K	π	σ_π	Ref.	M	N	S	σ_S	$\log(R'_{HK})$	$\sigma_{R'_{HK}} \times 10^5$	P_{rot}	S/N_{VR}
				[mas]	[mas]	Phot./ π	M/M $_\odot$						[d]	
GJ735	10.11	1.53	4.690	84.94	1.72	(1),(3)	0.64	1	7.062	0.000	-4.277	0.000	14	13.9
GJ740	9.21	1.46	3.820	91.68	1.54	(1),(3)	0.61	55	1.559	0.114	-4.625	0.203	24	28.3
GJ4092	10.92	1.27	3.742	38.50	2.30	(2),(3)	0.64	13	1.062	0.083	-4.793	0.158	31	15.6
GJ672.1	11.70	1.41	4.157	41.78	4.12	(2),(3)	0.52	4	1.051	0.466	-4.974	0.090	40	5.7
GJ4004	12.21	1.50	4.887	79.95	1.82	(2),(5)	0.31	3	1.072	0.289	-5.304	0.187	67	3.1
GJ4082	12.10	1.50	4.487	38.60	4.10	(2),(3)	0.54	2	1.465	0.119	-4.946	0.112	39	3.6
GJ739	11.23	1.36	4.506	70.95	2.56	(2),(3)	0.46	14	0.919	0.130	-5.218	0.121	59	9.6
GJ747.4	11.43	1.41	4.028	45.99	3.33	(2),(3)	0.51	11	1.250	0.161	-4.830	0.235	32	7.8
GJ762	12.14	1.35	4.346	38.72	1.34	(2),(5)	0.50	5	0.806	0.298	-5.226	0.322	59	4.5
GJ781.1A	12.55	1.50	5.129	67.08	5.02	(2),(3)	0.35	5	0.515	0.079	-6.030	0.040	202	5.6
GJ1252	12.25	1.41	4.311	50.53	2.14	(2),(5)	0.37	3	0.340	0.342	-5.356	0.357	72	4.2
GJ808	11.91	1.41	4.222	56.93	2.12	(2),(5)	0.37	5	0.407	0.197	-5.588	0.099	103	5.0
GJ9724	12.09	1.51	4.399	67.55	3.74	(2),(3)	0.31	6	0.510	0.076	-5.590	0.079	103	5.0
GJ9732	11.00	1.34	4.142	48.82	2.20	(2),(3)	0.59	8	1.666	0.211	-4.729	0.276	28	12.3
GJ838.6	12.02	1.50	4.420	68.33	3.84	(2),(3)	0.32	8	0.619	0.153	-5.443	0.154	83	7.5
GJ4293	11.50	1.36	4.026	39.90	3.04	(2),(3)	0.56	1	2.755	0.000	-4.434	0.000	18	11.2
GJ874	12.03	1.43	4.380	50.70	11.30	(2),(2)	0.42	5	0.900	0.128	-5.173	0.133	55	6.4
GJ4273	12.08	1.46	4.412	53.65	3.15	(2),(3)	0.39	3	1.242	0.176	-5.002	0.179	42	5.5
GJ865	11.48	1.61	5.050	75.87	5.83	(1),(3)	0.48	1	7.853	0.000	-4.380	0.000	16	4.4
GJ4303	11.59	1.40	4.148	40.34	2.84	(2),(3)	0.56	72	3.186	0.582	-4.416	0.758	17	7.3
GJ4332	11.12	1.36	4.014	37.92	2.23	(2),(3)	0.66	2	1.883	0.273	-4.613	0.403	23	7.1
GJ3025	11.09	1.30	3.821	28.93	1.91	(2),(3)	0.75	2	1.873	0.472	-4.533	0.838	21	6.0
GJ1012	12.17	1.47	4.957	75.40	5.10	(2),(2)	0.34	9	0.720	0.050	-5.607	0.030	106	8.7
GJ1032	12.30	1.46	4.668	44.29	3.02	(2),(3)	0.48	10	1.459	0.150	-5.028	0.120	44	7.3
GJ1030	11.53	1.42	4.347	45.23	2.29	(2),(3)	0.56	6	2.239	0.172	-4.669	0.186	25	8.4
GJ78	11.85	1.42	4.195	60.36	3.08	(2),(3)	0.35	7	0.384	0.066	-5.764	0.082	135	7.7
GJ3135	12.25	1.61	4.668	107.81	2.92	(2),(3)	0.20	11	0.774	0.155	-5.407	0.124	78	6.4
GJ3148A	12.10	1.50	4.945	69.81	3.10	(2),(3)	0.38	63	5.869	1.564	-4.468	0.957	19	5.8
GJ3139	11.86	1.46	4.577	50.68	2.53	(2),(3)	0.49	5	0.995	0.074	-5.203	0.065	57	7.6
GJ1051	11.98	1.38	4.034	36.41	4.51	(2),(3)	0.50	3	0.499	0.023	-5.418	0.034	80	7.8
GJ103	8.85	1.33	3.941	86.18	0.78	(2),(3)	0.75	1	0.656	0.000	-4.000	0.000	10	26.2
GJ3141	12.27	1.54	4.520	71.53	1.64	(2),(5)	0.28	10	0.400	0.116	-5.833	0.093	150	6.1
GJ1054A	10.34	1.19	3.949	52.08	2.13	(2),(3)	0.66	2	0.664	0.046	-3.982	0.618	10	14.4
GJ3212	11.69	1.42	3.985	29.00	8.70	(2),(3)	0.65	12	0.693	0.062	-5.155	0.095	53	10.0
GJ3131	11.27	1.32	4.475	64.10	19.20	(2),(3)	0.48	2	0.815	0.030	-5.279	0.029	64	10.3
GJ3160	12.12	1.38	4.515	38.45	3.15	(2),(3)	0.55	1	0.800	0.000	-5.310	0.000	68	3.2
GJ43	12.46	1.46	4.329	27.99	4.08	(2),(3)	0.58	7	0.539	0.206	-5.505	0.226	91	4.0
GJ3263	12.44	1.44	4.975	56.18	1.06	(2),(5)	0.41	17	0.625	0.148	-5.714	0.074	125	5.7
GJ3205	11.88	1.28	4.324	59.12	4.68	(2),(3)	0.38	20	0.744	0.132	-5.267	0.145	63	8.1
GJ3221	12.25	1.49	4.664	54.70	2.40	(2),(2)	0.40	28	3.769	0.707	-4.554	0.565	21	4.7
GJ3029	12.27	1.50	4.799	51.80	4.40	(2),(3)	0.44	1	11.559	0.000	-4.101	0.000	11	2.5
GJ3032	11.95	1.43	4.551	50.82	2.74	(2),(3)	0.47	4	0.827	0.152	-5.306	0.136	67	4.2
GJ1022	12.20	1.39	4.339	48.62	1.39	(2),(5)	0.40	9	0.508	0.111	-5.561	0.121	99	4.8
GJ3090	11.49	1.40	4.172	44.71	2.57	(2),(3)	0.54	1	3.171	0.000	-4.429	0.000	18	7.0
GJ9201	12.26	1.33	4.243	35.25	2.65	(2),(3)	0.50	10	0.876	0.191	-5.126	0.227	51	6.4
GJ143.3	12.39	1.44	4.459	43.71	6.44	(2),(3)	0.43	4	0.485	0.272	-5.581	0.210	102	3.7
GJ155.3	12.17	1.37	4.198	38.99	2.92	(2),(3)	0.47	12	0.691	0.085	-5.257	0.105	62	8.8
GJ3279	11.83	1.46	4.596	61.90	18.60	(2),(3)	0.41	11	0.809	0.082	-5.341	0.070	71	9.3
GJ3455	12.48	1.45	4.701	61.92	0.98	(2),(5)	0.32	12	0.533	0.089	-5.718	0.069	126	6.3
GJ333	12.16	1.57	4.190	72.50	16.30	(1),(2)	0.25	11	0.554	0.101	-5.413	0.127	79	7.1
GJ3500	11.94	1.55	5.043	72.80	1.30	(2),(5)	0.41	2	0.621	0.068	-5.779	0.038	138	7.4
GJ3020	11.66	1.38	4.524	43.89	4.39	(2),(3)	0.58	2	1.083	0.013	-5.129	0.012	51	4.6
GJ3009	12.15	1.53	4.731	57.10	17.10	(2),(3)	0.41	10	0.883	0.293	-5.350	0.220	72	5.0
GJ3293	12.03	1.42	4.520	42.60	12.80	(2),(3)	0.52	161	1.108	0.163	-5.114	0.149	50	6.6
GJ3563	12.04	1.50	4.521	63.47	3.54	(2),(3)	0.36	12	0.625	0.082	-5.487	0.075	88	8.7
GJ3527	11.90	1.38	4.819	73.70	22.10	(2),(3)	0.38	1	0.481	0.000	-5.895	0.000	165	4.1
GJ372	10.69	1.37	4.536	62.33	2.15	(2),(3)	0.63	1	1.247	0.000	-5.055	0.000	46	10.8
GJ3005	12.05	1.46	4.399	42.73	150.0	(2),(3)	0.49	1	1.277	0.000	-4.981	0.000	41	3.7
GJ3006	12.24	1.49	4.585	59.85	2.64	(2),(3)	0.35	7	0.812	0.237	-5.334	0.205	70	6.9
GJ179	11.96	1.59	4.990	81.38	4.04	(1),(3)	0.36	20	1.302	0.284	-5.233	0.094	60	7.7
GJ204.2	12.11	1.48	4.649	56.80	6.50	(2),(2)	0.41	10	0.894	0.146	-5.303	0.119	67	7.9
GJ3356	11.93	1.43	4.970	80.60	9.80	(2),(2)	0.36	10	1.003	0.081	-5.385	0.048	76	7.7
GJ3341	12.14	1.38	4.383	43.18	1.40	(2),(5)	0.46	132	0.752	0.196	-5.287	0.195	65	6.3
GJ1088	12.29	1.57	4.954	87.03	1.28	(2),(5)	0.28	2	1.075	0.478	-5.292	0.048	66	4.1
GJ238	11.62	1.55	4.520	60.77	1.94	(1),(3)	0.45	7	0.658	0.191	-5.430	0.089	81	7.9
GJ3404A	12.12	1.53	4.762	77.90	2.80	(2),(2)	0.31	11	0.620	0.056	-5.619	0.041	108	7.1

Table A.3. continued.

Name	V	B-V	V-K	π [mas]	σ_π [mas]	Ref. Phot./ π	M M/M _⊕	N	S	σ_S	$\log(R'_{HK})$	$\sigma_{R'_{HK}}$ $\times 10^5$	P_{rot} [d]	S/N_{VR}
GJ297.2B	11.88	1.46	4.438	44.50	8.90	(2),(2)	0.51	16	1.006	0.167	-5.133	0.166	51	7.4
GJ3470	12.38	1.40	4.367	44.60	13.40	(2),(2)	0.40	90	1.569	0.343	-4.857	0.363	34	4.3
GJ369	10.20	1.28	4.026	72.92	1.82	(2),(3)	0.55	45	0.787	0.095	-5.093	0.138	48	23.6
GJ3817	12.31	1.64	4.847	88.40	11.50	(2),(2)	0.26	9	0.817	0.169	-5.459	0.113	85	3.6
GJ660.1	11.71	1.34	3.749	50.10	3.62	(2),(3)	0.37	27	0.486	0.068	-5.299	0.129	66	9.6
GJ3598	12.51	1.49	4.464	35.90	10.80	(2),(3)	0.49	7	0.683	0.105	-5.393	0.102	77	4.3
GJ1212	12.04	1.52	4.763	53.41	4.76	(2),(3)	0.47	1	0.674	0.000	-5.555	0.000	98	4.9
GJ3634	11.99	1.46	4.496	50.55	1.55	(2),(5)	0.45	76	0.982	0.144	-5.173	0.135	55	7.7
GJ3918	12.54	1.51	4.685	62.30	18.70	(2),(5)	0.31	28	0.909	0.297	-5.310	0.233	67	4.9
GJ4005	12.16	1.51	4.481	51.60	15.50	(2),(5)	0.41	4	0.841	0.355	-5.262	0.338	63	3.9
GJ4056	11.93	1.46	4.419	73.20	22.00	(2),(5)	0.31	11	0.686	0.124	-5.368	0.125	74	9.6
GJ4088	11.51	1.33	3.921	36.20	10.90	(2),(5)	0.58	14	0.808	0.059	-5.030	0.095	44	11.8
GJ2121	12.34	1.42	4.718	44.58	5.36	(2),(3)	0.48	23	0.727	0.260	-5.467	0.170	86	4.6
GJ4016	12.28	1.53	4.409	47.50	14.30	(2),(3)	0.40	4	0.663	0.234	-5.357	0.144	72	4.3
GJ4065	12.37	1.42	4.979	95.40	1.90	(2),(2)	0.25	6	3.245	0.744	-4.761	0.440	29	3.0
GJ3643	12.43	1.51	4.609	50.90	4.58	(2),(3)	0.39	22	0.688	0.228	-5.457	0.182	85	4.2
GJ629.3	12.44	1.40	4.251	46.51	170.0	(2),(3)	0.36	13	0.519	0.241	-5.441	0.192	82	4.3
GJ4024	10.77	1.39	4.115	50.09	2.48	(2),(3)	0.63	2	2.721	0.565	-4.477	0.760	19	6.9
GJ2138	11.30	1.47	4.427	77.60	2.79	(2),(3)	0.39	7	0.812	0.146	-5.259	0.146	62	8.1
GJ4100	12.19	1.51	4.116	26.60	2.60	(2),(2)	0.61	8	1.693	0.229	-4.710	0.307	27	6.1
GJ1207	12.33	1.54	5.186	115.39	1.51	(2),(5)	0.23	1	5.579	0.000	-4.595	0.000	23	4.0
GJ9600	12.13	1.41	4.044	40.80	11.90	(2),(2)	0.42	1	0.619	0.000	-5.260	0.000	63	11.5
GJ723	11.23	1.81	3.746	30.49	7.89	(2),(3)	0.68	10	0.527	0.037	-5.235	0.071	60	11.5
GJ4077	12.11	1.46	4.528	72.80	21.80	(2),(3)	0.30	7	0.671	0.239	-5.394	0.172	77	5.0
GJ754.1B	11.73	1.48	4.292	91.30	4.00	(2),(2)	0.25	1	0.372	0.674	-5.044	0.000	45	4.7
GJ3700	12.40	1.41	4.505	55.70	16.70	(2),(2)	0.34	11	0.724	0.063	-5.372	0.059	74	8.7
GJ660A	11.48	1.46	4.800	98.19	12.09	(2),(3)	0.34	13	1.259	0.267	-5.169	0.187	54	6.1
GJ696	10.16	1.43	3.630	45.89	2.18	(1),(3)	0.69	33	1.646	0.122	-4.516	0.260	20	18.7
GJ4129	11.97	1.59	4.385	63.40	12.70	(2),(3)	0.35	3	0.407	0.111	-5.800	0.076	143	4.9
GJ4038	12.29	1.49	4.752	83.30	25.00	(2),(3)	0.27	1	0.879	0.000	-5.363	0.000	73	2.3
GJ730	10.73	1.45	3.870	47.08	2.12	(1),(3)	0.61	3	1.713	0.075	-4.599	0.127	23	10.6
GJ1248	12.27	1.47	4.378	73.80	1.90	(2),(2)	0.26	7	0.485	0.241	-5.464	0.192	85	3.9
GJ890	10.99	1.31	3.852	44.88	2.30	(2),(3)	0.57	1	0.701	0.000	-4.020	0.000	10	11.1
GJ891	11.34	1.46	4.321	62.17	3.27	(2),(3)	0.45	28	1.040	0.114	-5.060	0.126	46	11.4
GJ4331	11.32	1.34	3.990	29.93	2.52	(2),(3)	0.72	1	2.015	0.000	-4.569	0.000	22	6.0
GJ4310	10.86	1.22	4.027	49.22	2.02	(2),(3)	0.59	10	1.653	0.079	-4.684	0.115	26	14.3
GJ889.1	11.06	1.34	3.969	63.06	2.15	(2),(3)	0.43	3	0.595	0.079	-5.253	0.122	62	10.9
GJ4231	12.19	1.45	4.781	32.79	5.65	(2),(3)	0.66	1	0.961	0.000	-5.321	0.000	69	2.8
GJ4241	11.15	1.28	4.281	48.80	2.12	(2),(3)	0.59	4	1.642	0.067	-4.796	0.077	31	10.0
GJ4195	11.70	1.50	4.131	40.70	5.90	(2),(2)	0.53	4	0.507	0.148	-5.454	0.196	84	5.3
GJ4180	12.22	1.48	4.487	40.03	3.67	(2),(3)	0.50	6	1.432	0.246	-4.957	0.233	39	4.7
GJ4213	12.17	1.44	4.703	48.02	3.36	(2),(3)	0.48	2	3.192	0.694	-4.650	0.535	25	3.6
GJ9773	12.09	1.45	4.594	66.84	4.41	(2),(3)	0.34	4	0.739	0.233	-5.362	0.093	73	3.5
GJ843	12.09	1.47	4.881	78.20	11.70	(2),(2)	0.33	4	0.673	0.078	-5.619	0.051	108	5.9
GJ4249	12.10	1.47	4.264	48.42	4.51	(2),(3)	0.40	5	0.426	0.230	-5.633	0.215	111	4.4
GJ4253	12.45	1.45	4.386	42.30	12.70	(2),(3)	0.41	2	0.419	0.329	-5.381	0.249	75	4.0
GJ4262	12.23	1.42	4.388	45.10	13.50	(2),(3)	0.43	1	0.816	0.000	-5.237	0.000	60	3.6
GJ895.1	11.38	1.30	3.989	27.28	2.85	(2),(3)	0.75	4	1.410	0.109	-4.749	0.165	29	9.9
GJ4353	12.05	1.43	4.532	53.54	3.52	(2),(3)	0.42	4	5.100	1.263	-4.359	1.144	16	5.4
GJ817	11.45	1.49	3.920	52.16	2.92	(1),(3)	0.43	7	0.307	0.177	-5.881	0.086	161	7.5
GJ4197	12.26	1.42	4.603	64.30	19.30	(2),(3)	0.33	2	0.708	0.058	-5.436	0.049	82	5.1
GJ4383	11.80	1.44	4.713	59.47	2.70	(2),(3)	0.46	9	0.936	0.363	-5.304	0.277	67	6.4
GJ912	11.26	1.33	4.521	53.77	2.88	(2),(3)	0.57	8	1.344	0.208	-5.007	0.191	42	8.0
GJ4364	11.47	1.37	3.963	31.00	9.30	(2),(3)	0.67	11	1.113	0.107	-4.864	0.167	34	8.9
GJ828.2	11.17	1.47	3.980	61.18	2.39	(2),(3)	0.43	4	0.658	0.033	-5.188	0.050	56	12.0
GJ1099	11.98	1.48	4.522	68.70	13.70	(2),(3)	0.34	6	0.843	0.220	-5.280	0.202	64	6.6
GJ3508	11.90	1.32	4.555	52.74	3.69	(2),(3)	0.46	7	0.845	0.269	-5.294	0.238	66	7.2
GJ319C	11.76	1.54	4.460	66.96	3.91	(1),(3)	0.37	5	0.581	0.075	-5.513	0.073	92	7.8
GJ3492	11.96	1.46	4.639	66.70	20.00	(2),(3)	0.37	7	1.053	0.174	-5.198	0.142	57	6.1
GJ333.2A	12.39	1.41	4.550	47.70	8.00	(2),(2)	0.41	5	0.635	0.095	-5.490	0.084	89	6.8
GJ1077	11.90	1.53	4.660	65.35	1.91	(1),(5)	0.39	5	0.876	0.044	-5.321	0.036	69	5.9
GJ317	12.04	1.50	4.988	94.20	18.80	(2),(5)	0.30	23	1.127	0.085	-5.322	0.050	69	8.1
GJ816	11.34	1.43	4.624	69.53	2.93	(2),(3)	0.47	17	0.957	0.172	-5.249	0.143	61	9.0
GJ4149	11.70	0.64	4.047	37.20	10.98	(2),(3)	0.55	4	0.624	0.082	-5.256	0.118	62	5.0
GJ4155	12.10	0.50	4.374	47.60	14.30	(2),(3)	0.43	1	1.224	0.000	-4.992	0.000	42	5.9
GJ2033	11.04	1.42	4.285	46.82	4.32	(2),(3)	0.64	3	0.864	0.124	-5.154	0.142	53	6.9

Table A.3. continued.

Name	V	B-V	V-K	π	σ_π	Ref.	M	N	S	σ_S	$\log(R'_{HK})$	$\sigma_{R'_{HK}}$	P_{rot}	S/N_{VR}
				[mas]	[mas]	Phot./ π	M/M _⊕					$\times 10^5$	[d]	
GJ4362	12.41	1.52	4.643	41.25	1.55	(2),(5)	0.48	4	3.815	0.438	-4.540	0.358	21	6.6
GJ4159	11.55	1.39	3.860	36.36	3.15	(2),(3)	0.55	10	1.366	0.071	-4.710	0.121	27	8.1
GJ811.1	11.61	1.36	4.702	65.29	3.19	(2),(3)	0.46	2	1.144	0.133	-5.179	0.103	55	8.6
GJ864	9.99	1.44	3.700	58.42	1.79	(1),(3)	0.63	3	1.047	0.056	-4.782	0.112	30	19.2
GJ4265	11.91	1.33	4.170	37.67	3.50	(2),(3)	0.53	1	1.877	0.000	-4.681	0.000	26	4.9
GJ899	11.21	1.47	4.358	71.54	3.27	(2),(3)	0.43	5	0.561	0.018	-5.487	0.019	88	11.8
GJ4352	11.39	1.46	4.363	74.10	22.20	(2),(3)	0.38	4	0.450	0.072	-5.687	0.076	120	10.3
GJ4304A	11.36	1.32	4.096	40.89	2.12	(2),(3)	0.59	4	1.344	0.103	-4.821	0.141	32	9.3
GJ791	11.49	1.40	4.602	67.38	3.01	(2),(3)	0.45	2	0.873	0.035	-5.295	0.030	66	7.2
GJ810A	12.51	1.57	5.121	77.59	1.49	(2),(5)	0.31	1	0.558	0.294	-5.571	0.000	101	3.1
GJ812A	11.96	1.53	4.870	56.54	3.92	(1),(3)	0.48	9	3.651	0.503	-4.657	0.330	25	5.4